

























ALMA Survey of Orion Planck Galactic Cold Clumps (ALMASOP): The Warm–Envelope Origin of Hot Corinos

SHIH-YING HSU ^{1,2} SHENG-YUAN LIU ² DOUG JOHNSTONE ^{3,4} TIE LIU ⁵ LEONARDO BRONFMAN ⁶
HUEI-RU VIVIEN CHEN ⁷ SOMNATH DUTTA ² DAVID J. EDEN ⁸ NEAL J. EVANS II ⁹ NAOMI HIRANO ²
MIKA JUVELA ¹⁰ YI-JEHNG KUAN ^{11,2} WOJIN KWON ^{12,13} CHIN-FEI LEE ² CHANG WON LEE ^{14,15}
JEONG-EUN LEE ¹⁶ SHANGHUO LI ¹⁷ CHUN-FAN LIU ² XUNCHUAN LIU ¹⁸ QIUYI LUO ^{19,20} SHENG-LI QIN ²¹
MARK G. RAWLINGS ²² DIPEN SAHU ^{23,24} PATRICIO SANHUEZA ^{25,26} HSIEN SHANG (尚賢) ²⁷
KENICHI TATEMATSU ^{28,29} AND YAO-LUN YANG ³⁰

¹National Taiwan University (NTU), No. 1, Section 4, Roosevelt Rd, Taipei 10617, Taiwan (R.O.C.)

²Institute of Astronomy and Astrophysics, Academia Sinica, No.1, Sec. 4, Roosevelt Rd, Taipei 10617, Taiwan (R.O.C.)

³NRC Herzberg Astronomy and Astrophysics, 5071 West Saanich Rd, Victoria, BC, V9E 2E7, Canada

⁴Department of Physics and Astronomy, University of Victoria, Victoria, BC, V8P 5C2, Canada

⁵Key Laboratory for Research in Galaxies and Cosmology, Shanghai Astronomical Observatory, Chinese Academy of Sciences, 80 Nandan Road, Shanghai 200030, People's Republic of China

⁶Departamento de Astronomía, Universidad de Chile, Casilla 36-D, Santiago, Chile

⁷Department of Physics and Institute of Astronomy, National Tsing Hua University, Hsinchu, 30013, Taiwan

⁸Armagh Observatory and Planetarium, College Hill, Armagh, BT61 9DB, UK

⁹Department of Astronomy, The University of Texas at Austin, 2515 Speedway, Stop C1400, Austin, Texas 78712-1205, USA

¹⁰Department of Physics, P.O.Box 64, FI-00014, University of Helsinki, Finland

¹¹Department of Earth Sciences, National Taiwan Normal University, Taipei, Taiwan (R.O.C.)

¹²Department of Earth Science Education, Seoul National University, 1 Gwanak-ro, Gwanak-gu, Seoul 08826, Republic of Korea

¹³SNU Astronomy Research Center, Seoul National University, 1 Gwanak-ro, Gwanak-gu, Seoul 08826, Republic of Korea

¹⁴Korea Astronomy and Space Science Institute (KASI), 776 Daedeokdae-ro, Yuseong-gu, Daejeon 34055, Republic of Korea

¹⁵University of Science and Technology, Korea (UST), 217 Gajeong-ro, Yuseong-gu, Daejeon 34113, Republic of Korea

¹⁶Department of Physics and Astronomy, Seoul National University, 1 Gwanak-ro, Gwanak-gu, Seoul 08826, Korea

¹⁷Max Planck Institute for Astronomy, Königstuhl 17, D-69117 Heidelberg, Germany

¹⁸Shanghai Astronomical Observatory, Chinese Academy of Sciences, Shanghai 200030, PR China

¹⁹Shanghai Astronomical Observatory, Chinese Academy of Sciences, Shanghai 200030, People's Republic of China

²⁰School of Astronomy and Space Sciences, University of Chinese Academy of Sciences, No. 19A Yuquan Road, Beijing 100049, People's Republic of China

²¹Department of Astronomy, Yunnan University, and Key Laboratory of Astroparticle Physics of Yunnan Province, Kunming, 650091, People's Republic of China

²²Gemini Observatory/NSF's NOIRLab, 670 N. A'ohoku Place, Hilo, Hawai'i, 96720, USA

²³Physical Research laboratory, Navrangpura, Ahmedabad, Gujarat 380009, India

²⁴Academia Sinica Institute of Astronomy and Astrophysics, 11F of AS/NTU Astronomy-Mathematics Building, No.1, Sec. 4, Roosevelt Rd, Taipei 10617, Taiwan, R.O.C.

²⁵National Astronomical Observatory of Japan, National Institutes of Natural Sciences, 2-21-1 Osawa, Mitaka, Tokyo 181-8588, Japan

²⁶Department of Astronomical Science, SOKENDAI (The Graduate University for Advanced Studies), 2-21-1 Osawa, Mitaka, Tokyo 181-8588, Japan

²⁷Institute of Astronomy and Astrophysics, Academia Sinica, Taipei 10617, Taiwan

²⁸Nobeyama Radio Observatory, National Astronomical Observatory of Japan, National Institutes of Natural Sciences, 462-2 Nobeyama, Minamimaki, Minamisaku, Nagano 384-1305, Japan

²⁹Department of Astronomical Science, The Graduate University for Advanced Studies, SOKENDAI, 2-21-1 Osawa, Mitaka, Tokyo 181-8588, Japan

³⁰RIKEN Cluster for Pioneering Research, Wako-shi, Saitama, 351-0198, Japan

(Accepted August 14, 2023)

Submitted to ApJ

ABSTRACT

Hot corinos are of great interest due to their richness in interstellar complex organic molecules (COMs) and the consequent potential prebiotic connection to solar-like planetary systems. Recent surveys have reported an increasing number of hot corino detections in Class 0/I protostars; however, the relationships between their physical properties and the hot-corino signatures remain elusive. In this study, our objective is to establish a general picture of the detectability of the hot corinos by identifying the origin of the hot-corino signatures in the sample of young stellar objects (YSOs) obtained from the Atacama Large Millimeter/submillimeter Array Survey of Orion Planck Galactic Cold Clumps (ALMASOP) project. We apply spectral energy distribution (SED) modeling to our sample and identify the physical parameters of the modeled YSOs directly, linking the detection of hot-corino signatures to the envelope properties of the YSOs. Imaging simulations of the methanol emission further support this scenario. We, therefore, posit that the observed COM emission originates from the warm inner envelopes of the sample YSOs, based on both the warm region size and the envelope density profile. The former is governed by the source luminosity and is additionally affected by the disk and cavity properties, while the latter is related to the evolutionary stages. This scenario provides a framework for detecting hot-corino signatures toward luminous Class 0 YSOs, with fewer detections observed toward similarly luminous Class I sources.

Keywords: astrochemistry — ISM: molecules — stars: formation and low-mass

1. INTRODUCTION

The presence of interstellar complex organic molecules (iCOMs or COMs) in low-mass protostellar cores is of great interest. These COMs, organic species consisting of six or more atoms (Herbst & van Dishoeck 2009), such as methanol (CH_3OH), may play a role in habitability in planetary systems. Abundant (relative to molecular hydrogen $X > 10^{-8}$) saturated COMs have been found, since 2004, in the localized, warm (~ 100 K) and compact (~ 100 au) zones surrounding low- or intermediate-mass young stars, which are known as “hot corinos” (Ceccarelli 2004).

While earlier studies of hot corinos were more focused toward individual, often well-known and bright YSOs, such as IRAS 16293–2422 (Cazaux et al. 2003) and HH–212 (Codella et al. 2016; Lee et al. 2017), in recent years several chemical surveys toward low-mass protostellar objects have been conducted, leading to a greatly increasing number of the hot corino detection. Bergner et al. (2019), for example, found that three out of five low-mass Class 0/I protostars toward the Serpens cluster had hot-corino signatures. Belloche et al. (2020) observed 26 Class 0/I protostars, under the “Continuum And Lines in Young ProtoStellar Objects (CALYPSO)” Program, and report 12 sources harboring methanol. van Gelder et al. (2020) examined COM emission toward seven Class 0 protostellar cores in the Perseus Barnard 1 cloud and Serpens Main region and found three COM-rich sources. Yang et al. (2021) surveyed COMs toward 50 protostars in the Perseus cloud, under the “Perseus ALMA Chemistry Survey (PEACHES)” project, and 28 out of 50 sources appear to harbor warm methanol. Under the “ALMA Survey of Orion Planck Galactic Cold Clumps (ALMASOP)” project, Hsu et al. (2022) reported 11 sources having hot-corino signatures among 56 Class 0/I protostars. Most recently, Bouvier et al.

(2022) observed 19 protostars in the OMC-2/3 filament and detected five of them harboring hot corinos under the ORion ALMA New GEneration Survey (ORANGES).

Such sample studies, in contrast to the detailed investigations of individual objects, enabled the inspections of the nature of COM emission via statistical approaches. Belloche et al. (2020), for example, found that all sources showing hot-corino signatures in their sample have luminosities higher than $4 L_{\odot}$. The authors suspected that a lack of sensitivity might be producing the non-detections toward fainter sources, and therefore it remains unclear whether all low-mass protostars may go through a phase showing COM emission. Using the ALMASOP sample, Hsu et al. (2022) demonstrated a positive correlation between the YSO luminosity and both the emission extent and total amount of methanol molecules, which suggests that the detection of COM emission correlates with the size of the warm region in the protostellar system. Similarly, van Gelder et al. (2022) compiled the methanol data in literature studies toward 184 low- and high-mass protostars and found a positive correlation between the bolometric luminosities and the detected methanol (CH_3OH) mass. These characteristics are consistent with the contemporary paradigm of the hot corino, in which COMs formed on grain mantles and get thermally desorbed due to ice sublimation when the dust temperature reaches ~ 100 K (see, for example, Garrod & Herbst 2006; Garrod et al. 2008; Herbst & van Dishoeck 2009). The detection of the hot-corino signature at a given sensitivity therefore depends on the total amount of gas-phase COMs, such as methanol, which is related to the warm region’s size that is governed by the luminosity of the central YSO.

The luminosities, or correspondingly the resulting warm region sizes, of YSOs are likely not the only determining

factor in detecting their associated hot-corino signatures. In the ALMASOP sample, Hsu et al. (2022) found no hot-corino signatures in the Class I protostars, even though some of them have high bolometric luminosities comparable to those of the Class 0 protostars with COM emission. Indeed, the detection of hot corinos toward Class I protostars in the literature to date appear significantly rarer than that of Class 0 ones (dozens of Class 0 to only about ten Class I (e.g. SVS13-A (Lefèvre et al. 2017) and L1551-IRS5 (Mercimek et al. 2022)). Similarly, van Gelder et al. (2022) found that, at a given luminosity, in addition to YSOs with methanol masses following the empirical luminosity-mass correlation, there are also YSOs without methanol emission detection, suggesting additional factors other than luminosity at play.

The exact origin of the hot-corino signatures, which are diverse in the literature, may help investigate what physical parameters in addition to luminosity could govern the detectabilities of hot corinos. Jacobsen et al. (2019) suggests that the COMs reside in the “innermost envelope”, at 40 – 60 au of the embedded low-mass protostar L483 according to the extent of the COM emission and the non-detection of a Keplerian disk down to 15 au. Similarly, the Class 0 protostar B335 (Imai et al. 2016) appears to lack a Keplerian disk, at least down to 10 au (Yen et al. 2015). Furthermore, toward IRAS 16293-2422 A Oya et al. (2016) find that methanol (CH_3OH) and methyl formate (HCOOCH_3) concentrate around the inner part of the infalling and rotating envelope. Alternatively, put forward by Lee et al. (2017) and Lee et al. (2019a), the COM emission arises from the “disk atmosphere”, within a radius of ~ 40 au according to the spatially resolved images and the position-velocity (PV) diagrams of the protostar HH-212.

Do all solar-like protostars go through a phase showing a hot-corino signature? If so, is it possible to build a general picture for the detectability of hot corinos? In this study, we aim to answer these questions by identifying the origin of the hot-corino signatures in the ALMASOP sample.

We briefly introduce the ALMASOP observations and the sample selection for this study in Sect. 2. In Sect. 3, we present the YSO models for each source inferred from the Spectral Energy Distribution (SED) fitting and further show that the sources with hot-corino signature have relatively high envelope densities, high luminosities, and consequently, a large amount of warm envelope mass. In Sect. 4, comparisons between simulated and observed methanol emission images imply that the envelope dominates the COM emission in the observed sources. In Sect. 5, we review and highlight literature studies showing indicative signs of support for the warm envelope origin of COM emission and discuss the astrochemical implications of such a scenario. We outline our conclusions in Sect. 6.

2. ALMASOP PROJECT

The ALMASOP survey selected 72 clumps in the Orion A, B, and λ Orionis clouds as the observation targets, starting from a sample of Planck Galactic Cold Clumps (PGCCs, Planck et al. 2016) in the Orion Molecular Complex (Tatematsu et al. 2017; Liu et al. 2018; Yi et al. 2018; Eden et al. 2019; Tatematsu et al. 2020; Kim et al. 2020). The observations of the ALMASOP project were conducted with both the 12-m array (in two array configurations: C43-5 and C43-2 denoted, respectively, as TM1 and TM2) and the 7-m array (ACA/Morita Array) of the Atacama Large Millimeter/submillimeter Array (ALMA) as part of the Cycle 6 operations (#2018.1.003.2.S, PI: Tie Liu). Our observations contain four spectral windows (SPWs) centering at 216.6, 218.9, 231.0 and 233.0 GHz with a uniform bandwidth of 1875 MHz and a resolution of ~ 1.1 MHz. The imaging was carried out using the `tclean` task in Common Astronomy Software Applications (CASA, McMullin et al. 2007). Under the ALMASOP observation, Dutta et al. (2020) presents a sample of starless, prestellar, and protostellar cores. See Dutta et al. (2020) for more details about the ALMASOP observations.

3. YSO MODEL AND SED FITTING ANALYSIS

We aim to identify which YSO physical parameters might correlate with the (non-)detection of hot-corino signatures using our ALMASOP sample. We thus carry out an SED fitting analysis to derive the YSO models by a similar process to that introduced in Sect. 4 and Appendix C by Hsu et al. (2022). First, we select the sample for this study from the ALMASOP protostars based on their SED data points, including their fluxes and aperture radii at various wavelengths, as compiled by Dutta et al. (2020). Next, we employ a grid of YSO models and their corresponding SEDs at multiple wavelengths and aperture radii established by Robitaille et al. (2006). Finally, among the models in the grid, we identify the ones that best match with the observed SED data points.

3.1. SED Modeling Process

3.1.1. Sample Selection

We select the sample for this study from the ALMASOP protostars based on the corresponding SED data points tabulated in Table 6 of Dutta et al. (2020). These archival photometric data, covering wavelengths from $3.4 \mu\text{m}$ to $870 \mu\text{m}$, were collected from the Spitzer Space Telescope Survey of Orion A-B (Megeath et al. 2012), the Wide-field Infrared Survey Explorer (WISE, Wright et al. 2010), the AKARI/IRC All-Sky Survey Point Source Catalogue (AKARIPSC Ishihara et al. 2010), the Herschel Orion Protostellar Survey (HOPS, Stutz et al. 2013; Tobin et al. 2015), and the Atacama Pathfinder Experiment (APEX,

Stutz et al. 2013). The aperture radii for *Spitzer*, *Herschel*, and APEX measurements are quoted from Furlan et al. (2016) and the FWHMs of the beam for the WISE and AKARI measurements are based on Wright et al. (2010) and Ishihara et al. (2010), respectively. In addition, we append a SED data point at 1.3 mm using the integrated flux within twice the beam size in the continuum images made with the ALMASOP combined data (TM1+TM2+ACA). At 1.3 mm the missing flux due to interferometric observations could help with the situation by filtering out the very extended cloud component and being sensitive to only the core scale structures most relevant to the SED fitting. See Table A1 for more detailed information.

We further down-selected 16 Class 0 and seven Class I protostars based on the additional criteria below in order to have better-constrained the SED models:

1. We require photometric measurements for each source at mid-IR (3.4, 3.4, 4.5, 4.6 and 5.8 μm), far-IR (9, 12, 18, 22, 24, 70, 100, and 160 μm), sub-mm (350 and 870 μm), and mm (1,300 μm) bands, as they are sensitive to different components and mechanisms in a protostellar system (e.g., Whitney et al. 2003b; Robitaille et al. 2006; Furlan et al. 2016). In particular, we further require the source to have a photometric measurement at 100 μm at which the SED of Class 0/I protostars typically peak (see, for example, Furlan et al. 2016). Consequently, the sources in this study are all protostellar objects observed by the Herschel Orion Protostar Survey, (HOPS, Stutz et al. 2013; Tobin et al. 2015) from which we collected the 100 μm photometric data. These sources are distributed across the Orion A and B clouds.
2. The source is not blended with other sources in the [70 – 160] μm bands. Since ALMASOP has a better angular resolution than the other photometric literature data, sometimes more than one protostar identified in ALMASOP is part of the same HOPS object. To support the SED analysis and COMs investigation, we ensure that each selected YSO has only one-to-one corresponding HOPS counterpart cataloged by Furlan et al. (2016).

Overall, based on Dutta et al. (2020) catalogues, the 23 sources in our sample have a bolometric temperature range from 31 ± 10 K to 381 ± 60 K and a bolometric luminosity range from $0.4 \pm 0.2 L_{\odot}$ to $180 \pm 70 L_{\odot}$. Please refer to Table 1 for more information about the source coordinates, properties, and corresponding HOPS indices.

3.1.2. YSO Model Grid

For the physical parameters of the YSO models, we adopt the model grid published by Robitaille et al. (2006)

(hereafter, “R06 grid”). In the R06 grid, the SEDs were produced by HO-CHUNK¹, a Monte Carlo radiation transfer code for protostellar geometry from Class 0 to Class III sources (Whitney et al. 2003b,a). In HO-CHUNK, the YSO physical model consists of a central protostar, an infalling and rotating envelope, a flared disk, and a bipolar cavity. The envelope density model follows the “CMU” prescription (Ulrich 1976; Cassen & Moosman 1981). The disk density model is a standard flared accretion disk model (see, for example, Pringle 1981; Whitney et al. 2003b). Thus, the full physical model is axisymmetric and described by 14 parameters: stellar mass (M_{\star}), stellar radius (R_{\star}), stellar temperature (T_{\star}), envelope infall rate (\dot{M}_{env}), envelope outer radius ($R_{\text{env}}^{\text{outer}}$), cavity density (ρ_{cav}), cavity opening angle (θ_{cav}), disk mass (M_{disk}), outer disk radius ($R_{\text{disk}}^{\text{outer}}$), the inner radius of disk and envelope (R^{inner}), disk accretion rate (\dot{M}_{disk}), disk scale height factor ($z_{\text{disk}}^{\text{scale}}$), disk flaring power component (B_{disk}), and ambient density (ρ_{amb}). The R06 grid has 200,000 physical YSO models, each with 10 SEDs evaluated at different inclination values ($\cos \varphi$). More information of the R06 grid is available by Whitney et al. (2003b), Robitaille et al. (2006), Robitaille et al. (2007), and the instruction file of the HO-CHUNK package.

3.1.3. SED Fitting

We employed the SED Fitter² (Robitaille et al. 2007) for evaluating the YSO models best matching with the observation. An additional extinction, A_V , was set to be in the range of [0, 30] mag based on Furlan et al. (2016). The source distance, D , was fixed to be 398 pc and 404 pc, respectively, for sources in the Orion A and B clouds (Kounkel et al. 2018). For each combination of SED grid model, foreground extinction (A_V), and distance (D), the SED Fitter evaluates the “goodness of fit” based on the χ^2 value defined by:

$$\chi^2 \equiv \sum_{i=1}^{N_{\text{data}}} \left[\frac{\langle \log_{10} F_{\nu}(\lambda_i) \rangle - \log_{10} M_{\nu}(\lambda_i)}{\sigma(\langle \log_{10} F_{\nu}(\lambda_i) \rangle)} \right]^2, \quad (1)$$

where $F_{\nu}(\lambda_i)$ and $M_{\nu}(\lambda_i)$ are the observed flux density and the modeled flux density at a given wavelength λ_i within the corresponding observational aperture, respectively, and σ is the uncertainty of the logarithm of the flux. In addition to the χ^2 value, the continuum and molecular line images obtained with ALMASOP yield more constraints to the acceptable model. First, we set an upper limit of the disk outer radius ($R_{\text{disk}}^{\text{outer}}$) at 90 au for those without clear disk signatures in the C¹⁸O $J = 2 - 1$ moment-0 images. Second, we limited

¹ <https://gemelli.colorado.edu/~bwhitney/codes/codes.html>

² <https://sedfitter.readthedocs.io/en/stable/>

Table 1. Sample list in this study.

Name	α_{J2000}	δ_{J2000}	Cloud	Stage	T_{bol} (K)	L_{bol} (L_{\odot})	HOPS Index	Hot Corino
G205.46–14.56M1–A	05h46m08.6s	-00d10m38.49s	Orion B	Class 0	47±12	4.8±2.1	HOPS–317	
G205.46–14.56S1–A	05h46m07.3s	-00d13m30.23s	Orion B	Class 0	44±19	22±8	HOPS–358	○
G206.12–15.76	05h42m45.3s	-01d16m13.94s	Orion B	Class 0	35±9	3.0±1.4	HOPS–400	
G206.93–16.61W2	05h41m25.0s	-02d18m06.75s	Orion B	Class 0	31±10	6.3±3.0	HOPS–399	○
G208.68–19.20N1	05h35m23.4s	-05d01m30.60s	Orion A	Class 0	38±13	36.7±14.5	HOPS–87	★
G209.55–19.68S1	05h35m13.4s	-05d57m57.89s	Orion A	Class 0	50±15	9.1±3.6	HOPS–11	○
G209.55–19.68S2	05h35m09.1s	-05d58m26.87s	Orion A	Class 0	48±11	3.4±1.4	HOPS–10	
G210.37–19.53S	05h37m00.4s	-06d37m10.90s	Orion A	Class 0	39±10	0.6±0.3	HOPS–164	
G210.49–19.79W–A	05h36m18.9s	-06d45m23.54s	Orion A	Class 0	51±20	60±24	HOPS–168	★
G210.97–19.33S2–A	05h38m45.5s	-07d01m02.02s	Orion A	Class 0	53±15	3.9±1.5	HOPS–377	
G211.01–19.54N	05h37m57.0s	-07d06m56.23s	Orion A	Class 0	39±12	4.5±1.8	HOPS–153	
G211.01–19.54S	05h37m58.8s	-07d07m25.72s	Orion A	Class 0	52±8	0.9±0.4	HOPS–152	
G211.16–19.33N2	05h39m05.8s	-07d10m39.29s	Orion A	Class 0	70±20	3.7±1.4	HOPS–133	
G211.47–19.27S	05h39m56.0s	-07d30m27.61s	Orion A	Class 0	49±21	180±70	HOPS–288	★
G212.10–19.15S	05h41m26.2s	-07d56m51.93s	Orion A	Class 0	43±12	3.2±1.2	HOPS–247	
G212.84–19.45N	05h41m32.1s	-08d40m09.77s	Orion A	Class 0	50±13	3.0±1.2	HOPS–224	
G205.46–14.56S2	05h46m04.8s	-00d14m16.67s	Orion B	Class I	381±60	12.5±4.7	HOPS–385	
G205.46–14.56S3	05h46m03.6s	-00d14m49.57s	Orion B	Class I	178±33	6.4±2.4	HOPS–315	
G210.82–19.47S–B	05h38m03.4s	-06d58m15.89s	Orion A	Class I	74±12	0.4±0.2	HOPS–156	
G210.97–19.33S2–B	05h38m45.0s	-07d01m01.68s	Orion A	Class I	82±24	4.1±1.6	HOPS–144	
G211.16–19.33N5	05h38m45.3s	-07d10m56.03s	Orion A	Class I	112±16	1.3±0.5	HOPS–135	
G212.10–19.15N2–A	05h41m23.79s	-07d53m46.74s	Orion A	Class I	114±10	1.1±0.5	HOPS–263	
G212.10–19.15N2–B	05h41m24.0s	-07d53m42.22s	Orion A	Class I	160±30	1.1±0.5	HOPS–262	

NOTE— α_{J2000} and δ_{J2000} are the right ascension and declination, respectively, of the peak position in our combined 1.3 mm continuum observations. T_{bol} and L_{bol} are respectively the bolometric temperature and bolometric luminosity adopted from Dutta et al. (2020). In the last column (Hot Corino), the symbols “★” and “○” represent the hot corino sources discovered in the ACA-only data (Hsu et al. 2020) and the combined data (Hsu et al. 2022), respectively. The horizontal line separates the sources at the Class 0 (top) and Class I (bottom) stages, split by $T_{\text{bol}} = 70$ K. All the sources are found to be low-/intermediate-mass protostars based on the SED modeling analysis in this study.

References— L_{bol} and T_{bol} : Dutta et al. (2020); HOPS Index: Furlan et al. (2016); Hot Corino: Hsu et al. (2020) and Hsu et al. (2022)

the projected opening angle adapted from Dutta et al. (2020) and Hsu et al. (2020) for the sources showing clear bipolar outflow in their CO $J = 2 - 1$ moment-0 images. See Robitaille et al. (2007) and Appendix C of Hsu et al. (2022) for more details.

For statistical robustness, we select the nine best-fit models (i.e., the nine models having the lowest χ^2 values) for each source. Table A2 provides the model names from the R06 grid. For each source, we derive the weighted average and standard deviation of the inferred physical parameters based on the χ^2 values to illustrate the distribution of the parameters and their statistical uncertainties (Table A3). The weight for each model w_j is defined as:

$$w_j \equiv \frac{1}{\chi_j^2}, \quad (2)$$

3.2. Best-fit YSO Parameters

We show the distribution of YSO model parameters relevant to our discussion versus the total luminosity (L_{tot} , i.e., the sum of stellar luminosity and accretion luminosity) in Figure 1 and attach the distributions for the full set of (14) parameters in Appendix A (Figure A2) for completeness. For the ALMASOP sample, red circles and blue crosses represent the Class 0 protostars with and without hot-corino signatures (Hsu et al. 2020, 2022), respectively. The black crosses represent Class I protostars and there are no hot corinos detected within this group. The majority of the sources in our sample have modeled stellar masses M_{\odot} below $\sim 2 M_{\odot}$, with one exception having a modeled stellar mass M_{\star} of $\sim 4 M_{\odot}$. This suggests that our sample consists of low-/intermediate-mass YSOs. At first glance,

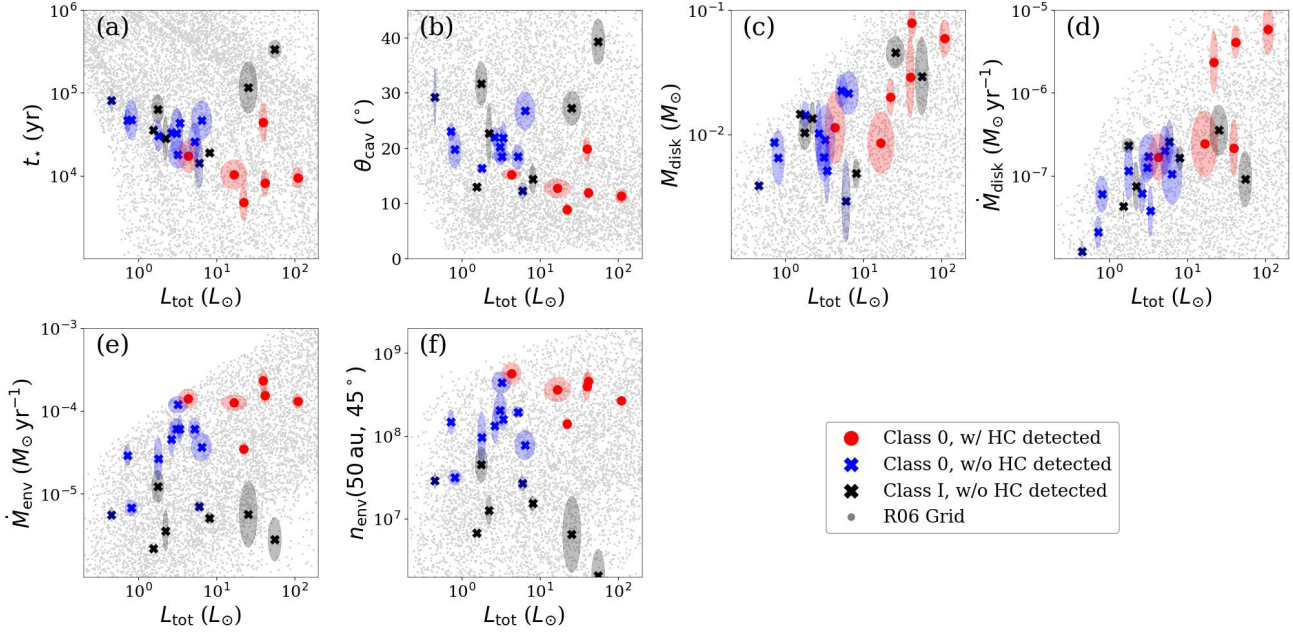


Figure 1. Weighted average and standard deviation of the following YSO model parameter versus total luminosity (L_{tot}). The t_* is the evolutionary age of the protostellar system. The θ_{cav} is the opening angle of the cavity. The M_{disk} is the total mass of the disk. The \dot{M}_{disk} is the disk accretion rate. The \dot{M}_{env} is the envelope infall rate. Panel (f) is the envelope number density at radius $r = 50$ au and polar angle $\theta = 45^\circ$. The red circles represent the sources with hot-corino signature (Hsu et al. 2020, 2022). The blue and black crosses represent the Class 0 and Class I protostars toward which hot corinos signatures are not detected, respectively. The grey dots represent all the YSO models in the R06 grid. Note that the last two YSO parameters are not the original R06 grid parameters.

there appear to be some noticeable correlations between certain physical parameters and the total luminosity. Some of these correlations are in fact related to the underlying grid sampling of the parameters, which is illustrated by the background, light gray markers in each panel. For example, the clear positive correlation between the stellar mass (M_*) and the total luminosity (L_{tot}) of our sample in Figure A2–(b) is intrinsically limited by the sampling.

3.3. Trends in parameters from Class 0 to Class I

The SED fitting approach admittedly has its limitations as it imposes very simplified YSO physical models. The lack of near-infrared (near-IR) photometric data also makes the stellar parameters such as stellar temperature and radius somewhat uncertain. However, the inferred total luminosity, which dictates the thermal structure, is mainly determined at $100 \mu\text{m}$ and will not be severely affected. By comparing the distributions of the inferred parameters of YSO sources at different stages, we find reasonable trends implying that valuable insight is offered by these parameters extracted from the SED fitting.

- Evolutionary age (t_*): As shown in Figure 1–(a), Class I protostars are more evolved than their Class 0 counterparts. The evolutionary ages of Class 0 protostars mostly range from 2.0×10^3 to 3.6×10^4 yr, while those of Class I protostars range from 2.5×10^4 to 3.2×10^5 yr. There seems to be a tentative transition

band between Class 0 and Class I protostars at $t_* \sim 2.5 \times 10^4$ yr, which is comparable to the estimation of $2 - 6 \times 10^4$ yr suggested by Froebrich et al. (2006).

- Cavity opening angle (θ_{cav}): As shown in Figure 1 (b), Class I protostars have larger cavity opening angles (θ_{cav}) being around 15° and above while Class 0 protostars have smaller opening angles ranging from a few degrees to around 20° . This is consistent with the results by Arce & Sargent (2006) and Seale & Looney (2008), that the outflow opening angle of a protostellar source becomes wider as the YSO evolves.
- Disk mass (M_{disk}): As shown in Figure 1–(c), there is no clear division in the disk mass (M_{disk}) between the Class 0 and I stage. This result appears to be consistent with Jørgensen et al. (2009) and Tobin et al. (2020) in which no obvious growth of disk masses from Class 0 to Class I stage was found.
- Disk accretion rate (\dot{M}_{disk}): As shown in Figure 1–(d), the disk accretion rates for Class 0 protostars span mostly from 10^{-7} to $10^{-5} M_\odot \text{yr}^{-1}$. For Class I protostars, the disk accretion rates range from 10^{-8} to $10^{-6} M_\odot \text{yr}^{-1}$. These results are consistent with Fiorellino et al. (2021) and Fiorellino et al. (2023). The declining mass accretion rate from the Class 0 to the

Class I stage is also hinted at by [Yen et al. \(2017\)](#) based on their observations as well as literature.

We note that while G211.16–19.33N2 and G210.82–19.47S–B have bolometric temperatures (T_{bol} of 70 ± 20 and 74 ± 12 K, respectively) at the borderline between the Class 0 and Class I categories, the trends discussed above remain valid. In addition, we examine and comment on the validity of our SED modelling for five fields with the presence of multiplicity reported by the VLA/ALMA Nascent Disk and Multiplicity (VANDAM) survey of Orion protostars ([Tobin et al. 2020](#)). In the cases of G205.46–14.56M1–A (HOPS–317) and G205.46–14.56S1–A (HOPS–358), the separations between the two components (HOPS–317–A/B and HOPS–358–A/B, respectively) exceed 2,000 au. Only the A components are registered as the HOPS objects and the SED measurements are also dominated by the A components. Our modelling is thus applicable to the A components in these two systems. In the cases of G210.49–19.79W–A (HOPS–168) and G206.12–15.76 (HOPS–400), the separations between the two components (HOPS–168–A/B and HOPS–400–A/B, respectively) are ~ 100 au. Their SED measurements are likely dominated by the A components, as they are 1.5–5 times brighter than their counterparts in the VANDAM survey. Moreover, their CO outflows observed by ALMASOP are primarily associated with the brighter components. Our modelling is therefore also applicable to the A components in these two systems. Lastly, G211.47–19.27S (HOPS–288) was reported by the VANDAM survey as a triple system (HOPS–288–A–A, HOPS–288–A–B, and HOPS–288–B), with a very close separation of ~ 50 au between HOPS–288–A–A/B and an intermediate distance of ~ 200 au to HOPS–288–B. It is not fully obvious from which component the CO outflow(s) reported by ALMASOP is originated. Given the close proximity of the triple system, our SED fitting result is more likely a descriptive model for the envelope of the circumbinary (HOPS–288–A–A/B) or the circum-triple system.

3.4. Hot Corino and Envelope Infall Rate, Density, and Mass

At high luminosities, namely modeled total luminosity $L_{\text{tot}} > 5L_{\odot}$, we further find that the envelope infall rate (\dot{M}_{env}) exhibits a trend between sources with and without hot-corino signatures. As shown in Figure 1–(e), The envelope infall rates (\dot{M}_{env}) for Class 0 and Class I YSOs are clearly differentiated, with those of Class 0 YSOs ($\sim 5 \times 10^{-5} M_{\odot} \text{ yr}^{-1}$) being significantly higher than those of Class I YSOs ($\sim 5 \times 10^{-6} M_{\odot} \text{ yr}^{-1}$). These values are comparable to the median envelope infall rates obtained by [Furlan et al. \(2016\)](#) ($\sim 2.5 \times 10^{-5}$ and $\sim 1.0 \times 10^{-6} M_{\odot} \text{ yr}^{-1}$ for Class 0 and Class I YSOs, respectively). This differentiation presents a potential connection between

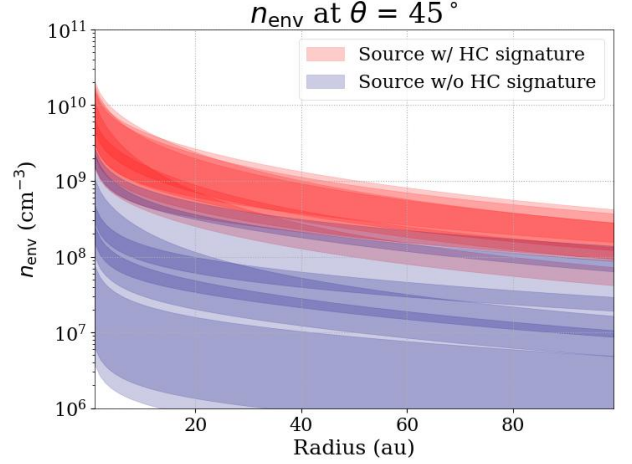


Figure 2. The number density profile from the “CMU” envelope models. Each color band represents an individual source in our sample at modeled total luminosity $L_{\text{tot}} > 5 L_{\odot}$.

envelope infall rate and COM emission intensity. The COM emission intensity presumably correlates with the total amount of gaseous COMs. The total amount of gaseous COMs should positively correlate with the warm envelope mass if COMs thermally desorb into the gas-phase within the envelope due to ice sublimation at ~ 100 K. Thus, the warm envelope mass is in turn related to the envelope infall rate.

The envelope density model in HO-CHUNK is the “CMU” model ([Ulrich 1976](#); [Cassen & Moosman 1981](#)), in which the circumstellar material is freely falling with a slight rotation and the trajectories terminate at the disk midplane. The envelope density ρ_{env} at radius r and polar angle θ in the “CMU” model is:

$$\rho_{\text{env}}(r, \mu) = \rho_{\text{env},C} \left(\frac{r}{R_C} \right)^{-3/2} \times \left(1 + \frac{\mu}{\mu_0} \right)^{-1/2} \left(\frac{\mu}{\mu_0} + \frac{2\mu_0^2}{r/R_C} \right)^{-1}, \quad (3)$$

where R_C is centrifugal radius (same as the outer radius of the disk $R_{\text{disk}}^{\text{outer}}$ in the R06 grid), $\mu = \cos \theta$, μ_0 is the value of μ for the streamline of infalling particles as $r \rightarrow \infty$, satisfying:

$$\frac{r}{R_C} = \frac{1 - \mu_0^2}{1 - \mu/\mu_0}, \quad (4)$$

and the characteristic density factor $\rho_{\text{env},C}$ is defined by:

$$\rho_{\text{env},C} = \frac{M_{\text{env}}}{4\pi R_C^3} = \frac{\dot{M}_{\text{env}}}{4\pi (GM_{\star} R_C^3)^{1/2}}, \quad (5)$$

where M_{env} is envelope mass, \dot{M}_{env} is envelope mass infall rate, and M_{\star} is the stellar mass. Note that a singularity in $\rho_{\text{env},C}$ occurs in the midplane at the centrifugal radius (R_C).

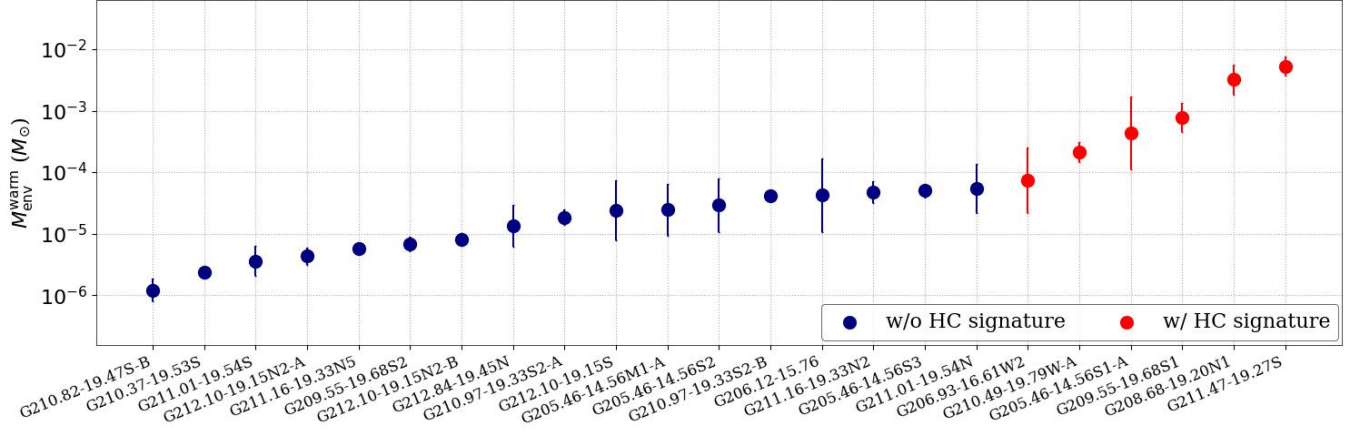


Figure 3. The warm envelope mass inferred from the nine best-fit model physical parameters. The red and navy dots represent the sources with and without hot–corino signatures (Hsu et al. 2020, 2022).

We evaluate the nominal envelope number density ($n_{\text{env}} = \rho_{\text{env}}/m_{\text{H}_2}$, where m_{H_2} is the mean molecular hydrogen mass) at radius $r = 50$ au (half of the typical hot corino size) and polar angle $\theta = 45^\circ$ (to avoid outflow cavity and singularity in the midplane) for all the R06 grid, which includes the sets of best-fit models for the ALMASOP sample. As shown in Figure 1–(f), the Class I sources generally have lower envelope density than the Class 0 sources. This differentiation is particularly evident at high luminosities, where Class 0 YSOs show hot–corino signatures but Class I YSOs do not. In Figure 2, we compare the envelope molecular gas number density profile at polar angle $\theta = 45^\circ$ (to avoid outflow cavity and density singularity in the midplane) for sources with modeled total luminosity $L_{\text{tot}} > 5 L_{\odot}$ (the lower limit for our sources with hot corino detected). The differentiation between the sources with and without hot–corino signatures in our sample is generally valid. We note again that this envelope density value is an indicator of the envelope density level.

To take into account the overall physical structure and compute the warm envelope mass, we run the HO–CHUNK simulations for our sample and then integrate the density within the following region: (1) having a temperature higher than 100 K (ice sublimation temperature) and (2) being outside the disk-dominant region (within three times of the disk scale height) or the cavity interior. As shown in Figure 3, the sources with hot–corino signature indeed have high warm envelope mass.

4. METHANOL EMISSION IN WARM ENVELOPES

Our SED analysis favors the hypothesis that COM emission leading to the hot–corino signature originates from a warm envelope. To verify whether the existence of COMs in an envelope can produce emission consistent with actual observations, we carried out imaging simulations of CH_3OH emission based on the previous SED model parameters.

We select the three most luminous sources (in terms of either their observed bolometric luminosity, the averaged total luminosity from the nine best-fit models, or their total luminosity from the best-fit model) in which hot corinos have been detected in the ALMASOP project (Hsu et al. 2020, 2022), namely G208.68-19.20N1 (HOPS–87), G210.49-19.79W–A (HOPS–168), and G211.47-19.27S (HOPS–288), for the simulation, hereafter G208N1, G210WA, and G211S, respectively.

4.1. Physical Parameters

We first use HO–CHUNK to calculate the thermal structure, namely, the temperature profile based on the best-fit YSO model exported by the SED Fitter. Refer to Table A4 for the parameters used in the HO–CHUNK simulations.

Figure 4–(a) and –(b) show the model-derived gas number density and the temperature distribution, respectively, for the three sources. The flaring disks dominate the inner densest regions near the midplane, and the warm bipolar regions are due to the outflow cavities. As found by Whitney et al. (2003b), the outer midplane is relatively cooler since the optically thick disk blocks much of the stellar radiation. In contrast, the bipolar cavity is relatively warmer due to its direct radiation exposure. Based on these thermal structures, we next determine the distribution of gas-phase methanol. We assume that the entire warm (i.e., $T > 100$ K, the ice sublimation temperature) region, excluding the cavity interior, harbors gaseous CH_3OH , the most commonly-detected COM.

4.2. Image Simulation of Methanol Emission

We use SPARX³ (Simulation Package for Astronomical Radiative Xfer), a radiative transfer code for calculating molecular line and dust continuum radiation, to produce

³ <https://sparx.tiara.sinica.edu.tw/>

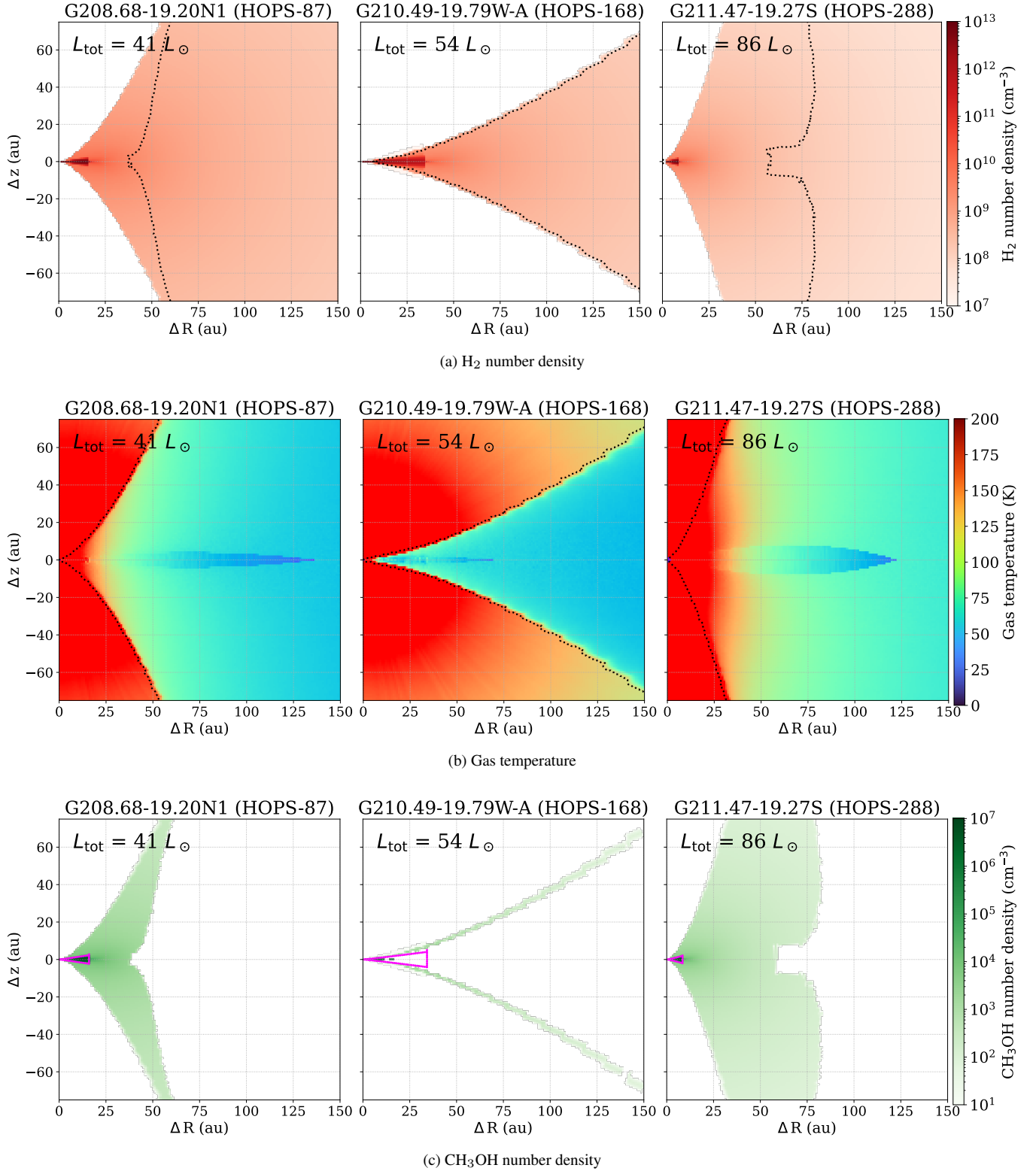


Figure 4. The molecular hydrogen number density (a), gas temperature (b), and methanol number density (c) maps for the three sources where hot corinos were ACA-detected. The text in the upper left corner of each panel shows the total luminosity of the best-fit model exported by the SED Fitter. The dotted contours in the top panels (a) show the location where the gas temperature attains 100 K. The dotted contours in the middle panels (b) illustrate the edge of the outflow cavities. The shadowed regions in the bottom panels are the areas between the dashed contours in (a) and (b), while the color scale represents the number density of methanol. The magenta dotted lines in the bottom panels (c) illustrate the disk-dominant boundaries, set at three times of the disk scale height. At the disk outer radius ($R_{\text{disk}}^{\text{outer}}$), the disk-dominant boundaries are of 2.4, 4.2, and 2.1 au, respectively, in their vertical heights.

synthetic CH₃OH image cubes with the number density and temperature profiles exported by HO-CHUNK (Sect. 3). Following the approach detailed in HO-CHUNK (Whitney et al. 2003b) and used by Keto & Zhang (2010), we adopt the gas velocity in the infalling envelope via the “CMU” (Ulrich 1976; Cassen & Moosman 1981; Mendoza et al. 2004) model, and assume that the gas velocity in the disk follows a Keplerian velocity. We set a fixed fractional abundance (i.e., the relative number density with respect to H₂) of gas-phase CH₃OH of $X = 10^{-6}$ for all sources. This abundance is comparable to that of $\sim 10^{-7}$ – 10^{-6} determined by Hsu et al. (2022) and to the CH₃OH abundance found in ices (Boogert et al. 2015; Brunken et al. 2022). The methanol line that we chose for the demonstration is the E-CH₃OH 4(2, 3)–3(1, 2) transition, which is the strongest methanol transition in the ALMASOP observations having upper energy $E_{\text{up}} = 46$ K and rest frequency $f_{\text{rest}} = 218440.0$ MHz. The level populations are assumed to be under local thermodynamic equilibrium (LTE), as the modeled H₂ number density is well-above the critical density at $\sim 10^6$ cm⁻³ of this transition.

4.2.1. Envelope+disk case

As noted previously, the YSO physical model consists of a central protostar, an infalling and rotating envelope, a flared disk, and a bipolar cavity. In the “envelope+disk” case, the gas-phase COM emission will arise from the (inner) warm disk and the envelope surface below the outflow cavity, forming a bipolar cone-shaped shell, as shown in Figure 4–(c).

To compare the resulting synthetic CH₃OH image cubes with the ALMASOP observational maps, we further made simulated maps by subtracting the synthetic (line-free) continuum image from the image cubes, convolving the continuum-subtracted cubes with the ALMASOP elliptical beam (the geometric mean $\overline{\text{HPBW}}$ is of $\sim 0''.45$, or ~ 180 au at a distance $d = 400$ pc. See Table A3). We made the moment–0 maps within the velocity intervals based on the line width reported by Hsu et al. (2022) around the line center and imposed a simulated noise level consistent with the real observations. Given that the CH₃OH emission is compact in all cases, we expected negligible missing flux due to lack of short baselines, and therefore carry out imaging simulations without employing the “simobserve” task in Common Astronomy Software Applications package (CASA).

Figure 5–(a) shows the simulated moment–0 maps of the CH₃OH emission for the “envelope+disk” case, and Figure 5–(b) shows the ALMASOP observed spectral images for the same sources based on their best–fit YSO models. We apply 2D Gaussian fitting to the integrated CH₃OH emission images in both sets of maps. In each panel of Figure 5–(a) and –(b), the aqua ellipse illustrates the full–width–

Table 2. Comparison between SPARX simulation and ALMASOP observation

Source	FWHM		Peak	
	(")		(mJy beam ⁻¹ km s ⁻¹)	
	SPARX	ALMASOP	SPARX	ALMASOP
G208N1	0''.50 ± 0''.02	0''.41 ± 0''.01	623 ± 227	321 ± 4
G210WA	0''.72 ± 0''.05	0''.45 ± 0''.03	145 ± 70	834 ± 36
G211S	0''.62 ± 0''.04	0''.67 ± 0''.03	1706 ± 356	2340 ± 54

NOTE— The transition is the CH₃OH-46 transition. The methanol abundance model in SPARX is the “envelope+disk” model. The result for SPARX are the weighted average and standard deviation for the nine best–fit YSO models.

half–maximum (FWHM) of the image and the label shows geometric mean of the FWHMs. Moreover, we consider all nine best–fit YSO models for the three sources and calculate the weighted average and standard deviation of the simulated methanol emission peak intensity and size. As summarized in Table 2, with a fixed CH₃OH fractional abundance $X = 10^{-6}$, the differences between the SPARX imaging simulations and the ALMASOP observation are in general less than a factor of two, both in terms of the integrated intensity and the emission extent. The only major difference appears in the integrated intensity for the case of G210.49–19.79W–A, which is a factor of six. Such a discrepancy might be caused by a relatively higher fractional abundance of methanol X in the source, which is fixed to 10^{-6} in the imaging simulation.

4.2.2. Disk case

The above “envelope+disk” cases reproduce well the observed CH₃OH emission. To examine whether the CH₃OH emission is predominantly from the disk or from the envelope, we further generated simulated maps for “disk”-only cases in which gas-phase methanol molecules just reside in disk regions. In other words, different from the “envelope+disk” case, we only consider methanol within three times the scale height above and below the disk midplane, as illustrated by the magenta dashed curves in Figure 4–(c).

As shown in Figure 5–(c), the simulated CH₃OH integrated intensity images for these “disk” cases appear quite different from the observed moment-0 maps. The simulated methanol integrated emission is even below the noise level of the observations. For the “disk” cases in general, despite gas phase CH₃OH residing in the disks, the modeled CH₃OH spectral emission is either too compact and

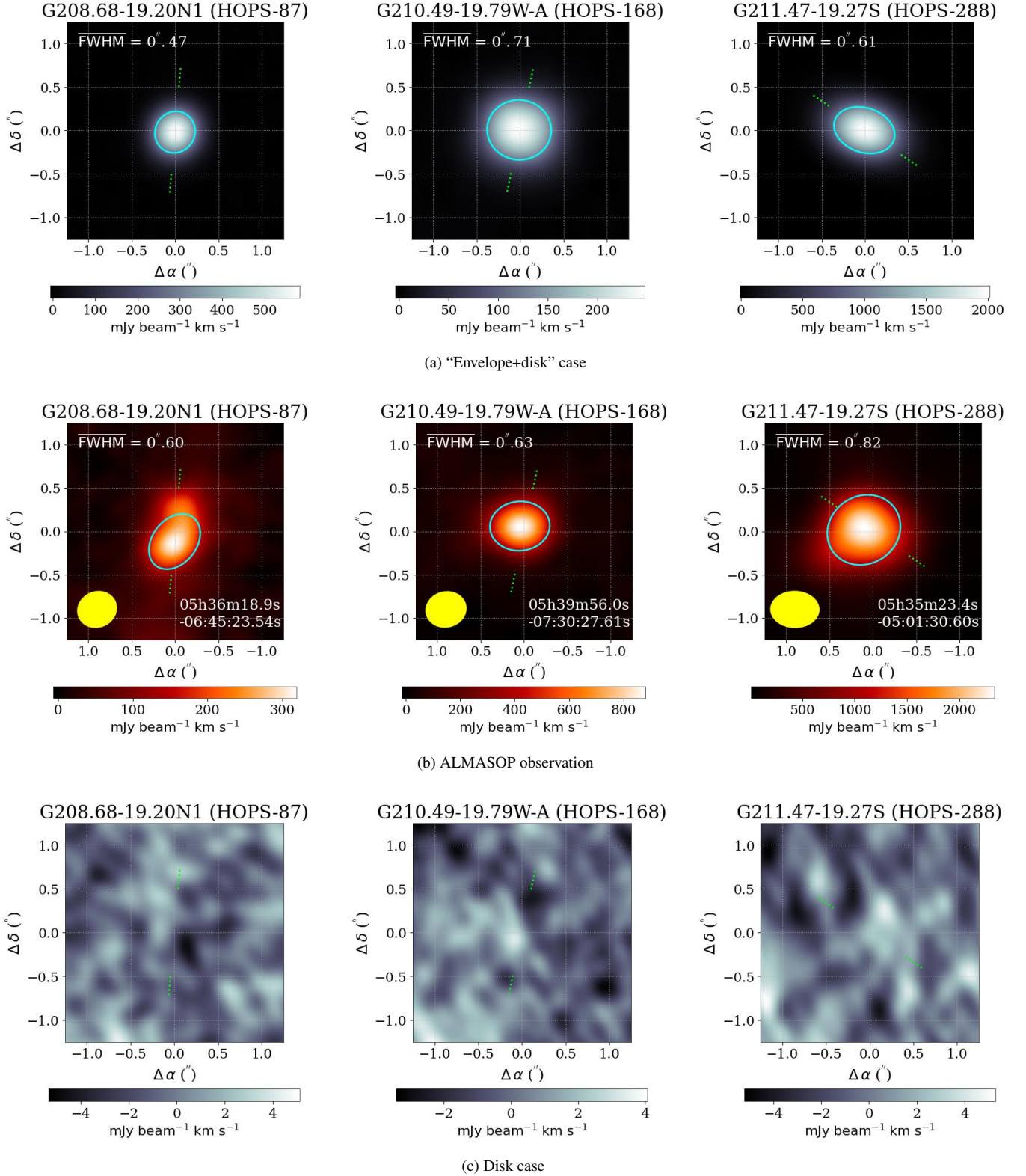


Figure 5. The top (a) and the bottom (c) panels are the SPARX simulation results for the “envelope+disk” case and the “disk” case. The middle (b) panels are the observed data from ALMASOP, and the center coordinates are labeled at the bottom right corners. The x-axes and the y-axes are the relative right ascension ($\Delta\alpha$) and the relative declination ($\Delta\delta$), respectively. The aqua ellipse illustrates the FWHM from 2D Gaussian fitting, and the geometric mean of the FWHM is shown at the top of each panel. Please refer to Table 2 for more details of the 2D Gaussian fitting result. The lime dashed lines show the cavity axis (Dutta et al. 2020; Hsu et al. 2022). The two rightmost panels in the bottom row have no 2D Gaussian fitting result since their integrated intensities are too weak.

weak or getting veiled by the very dense and consequently optically-thick dust continuum.

In summary, the lack of correlation between the disk parameters and the presence of hot-corino signatures, as indicated in Sect. 3, implies that the COM emission does not originate from only disks in these objects. Moreover, the “envelope+disk” cases reproduce the ALMASOP CH₃OH results much better, which implies that CH₃OH in the warm envelope is likely responsible for the observed COM emission.

5. DISCUSSION

5.1. Warm-envelope Origin of Hot Corino

Our findings, including the correlation between the corino detection and the warm envelope mass and the detailed imaging simulation strongly favors the hypothesis that the warm COM emission seen in the ALMASOP sample originates within the YSO warm envelope. This “warm-envelope” scenario follows the thermal desorption paradigm, in which COMs thermally desorb from dust grains when the temperature exceeds the ice sublimation temperature at ~ 100 K (e.g., Garrod & Herbst 2006; Garrod et al. 2008; Herbst & van Dishoeck 2009). The central protostar is crucial in heating the surrounding environments, including the circumstellar envelope and the Keplerian disk. However, the disk-shadowing effect, as depicted in 4–(a) and –(b) leads to lower temperatures in the regions near the midplane, resulting in a reduced warm region within the envelope and particularly the disk. Such disk-shadowing effect, for example, has been observed by Murillo et al. (2015) toward the Class 0 protostar VLA 1623A and demonstrated by Nazari et al. (2022) through the comparison between their “envelope-only” models and “envelope-plus-disk” models. In contrast, as shown in Figure 4–(a) and –(b), regions in the envelope further away from the midplane are less affected by the disk-shadowing effect. Additionally, as indicated by Figure 4–(a) and –(b), photons emitted by the central protostar can penetrate the outflow cavities and heat up the envelope. Without an outflow cavity, the warm region size in the envelope may be significantly reduced. As a result, the envelope component predominates the warm region in a protostellar system and leads to the dominance of the observed hot-corino signature.

In the “warm-envelope” scenario, the detectability of gaseous COMs is predominately dictated by both the luminosity and the envelope density profile. A higher YSO luminosity leads to a broader region harboring gas-phase COMs, as demonstrated by Hsu et al. (2022). Furthermore, the higher envelope density (with a fixed fractional abundance) results in a greater amount of COMs. At a fixed observing sensitivity, a Class 0/I protostar having a more massive warm envelope will give rise to more intense

COM emission, making the hot corino in this protostar more easily detectable.

The common warm-envelope origin found in the ALMASOP sample implies that any Class 0/I protostars could harbor a hot corino, provided that their inner envelope reaches a sufficient temperature, as was initially suggested by Ceccarelli (2004). Consequently, with appropriate observations, such as a high-sensitivity census of CH₃OH toward protostars with yet-detected hot corinos, it is likely that the majority of Class 0/I protostars will exhibit hot-corino signatures. The warm-envelope origin can be verified by not only spatially resolved imaging but also accurate kinematics allowing precise position-velocity (PV) diagrams.

Before such observations are achieved, it is worthwhile to examine whether the above warm-envelope scenario discovered in ALMASOP could be generalized to the hot corino detection in other studies. In the following, we discuss results in the literature showing indicative signs of support to the scenario.

5.1.1. The Luminosity and the Radius of COM Extent

For a sample of protostars having comparable envelope densities (e.g., all at Class 0 stage), the COM emission extent is expected to be positively correlated with source luminosity, as is indeed suggested by Hsu et al. (2022). Results reported in the literature well-constraining the COM extent for hot-corino sources, L483 and B335, also suggest similar trends. Both L483 and B335 are nearly edge-on (i.e., inclination angle $\varphi \geq 80^\circ$) Class 0 protostellar cores lacking detected Keplerian disk. L483, located in the Serpens-Aquila Rift with a bolometric luminosity, $L_{\text{bol}} = 10.5 L_\odot$ was found to exhibit COM emission at a scale of 40 – 60 au. (Shirley et al. 2000; Oya et al. 2018; Jacobsen et al. 2019). Jacobsen et al. (2019) attributed this emission to the innermost warm envelope. B335, in Bok globule B335, has a relatively low bolometric luminosity ($L_{\text{bol}} = 1.36 L_\odot$), and the COM distribution remains unresolved at a scale of ~ 45 au (or HPBW=0''.55 at a distance $d \sim 165$ pc, Hirano et al. 1988; Yen et al. 2010; Imai et al. 2016; Watson 2020; Evans et al. 2022). There exist luminosity variations in B335 (Evans et al. 2022), which have admittedly led to variations in the warm region size.

5.1.2. The envelope density of Class I Protostars with Hot Corino Detected

A Class I protostar generally has a lower envelope density than a Class 0 protostar, which based on our hypothesis, would make the detection of COM emission toward a Class I protostar more difficult. In our ALMASOP sample, for example, the modeled envelope number densities at our nominal reference location, $r = 50$ au and $\theta = 45^\circ$, of all Class I protostars are below $3 \times 10^8 \text{ cm}^{-3}$, as shown in Figure 1–(f). Even though some of them have high

luminosities and narrow cavity angles (e.g., $L_{\text{tot}} \sim 30L_{\odot}$ and $\theta_{\text{cav}} \sim 27^{\circ}$ for G205.46–14.56S3), no hot-corino signatures were detected toward them. Besides, Lindberg et al. (2014) and Artur de la Villarmois et al. (2018) interpreted the non-detection of CH₃OH emission toward protostellar cores R Cra–IRS 7B (a borderline Class 0/I protostar at $4.6 L_{\odot}$) and Oph–IRS 67 (a Class I binary protostellar system at $4.0 L_{\odot}$) as a result of the low density in their warm inner envelopes because of the presence of a disk and the consequent flat envelope density profiles.

However, Class I protostars with high envelope densities may change such a situation. For example, both Ser–emb 17 and L1551–IRS5, having their average cavity opening angles also less than 45° (Bergner et al. 2020; Wu et al. 2009), are Class I protostellar cores exhibiting hot-corino signatures. Ser–emb 17 has an envelope mass (M_{env}) of $3.6 M_{\odot}$ (Enoch et al. 2011; Bergner et al. 2019). Assuming a centrifugal radius $R_C \sim 100$ au, at the nominal reference location, the estimated envelope density would be $2.2 \times 10^{10} \text{ cm}^{-3}$ (Equation 3), which is even higher than those of the ALMASOP sources showing hot-corino signatures in Figure 1–(g). Similarly, for L1551–IRS5, Osorio et al. (2003) presented a protostellar model consisting of a flattened infalling envelope surrounding a binary system with individual circumstellar disks and a circumbinary disk through SED fitting. The reported envelope mass and the centrifugal radius are of $4 M_{\odot}$ and 300 au, respectively. By adopting these two parameters, we estimate that the corresponding envelope number density at the reference location is $1.7 \times 10^9 \text{ cm}^{-3}$ (Equation 3), comparable to those of sources with hot-corino signatures in ALMASOP, as indicated in Figure 1–(g).

5.1.3. The sensitivity and the presence of hot-corino signature

The hot-corino signatures of YSOs with higher luminosities are more likely to be detected at a given observational sensitivity if their envelope densities are comparable. This implication results from the fact that the sources with hot-corino signature in ALMASOP are mostly, if not all, Class 0 YSOs at the highest luminosities among the whole sample of Class 0 protostars. This picture also appears applicable to archival Class I hot corino surveys. Bergner et al. (2019), for example, observed two Class I protostars; among the two, Ser–emb 17 with the detection of COM emission has a significantly higher luminosity (of $3.8 L_{\odot}$) than the other (of $0.4 L_{\odot}$) with no COM emission detected. Mercimek et al. (2022) conducted a chemical survey of four Class I protostars distributed in the Taurus and Perseus clouds. Of the four Class I protostars, only L1551–IRS5, having the highest bolometric luminosity ($30 - 40 L_{\odot}$ for L1551–IRS5 and $3.5 - 5.0 L_{\odot}$ for others), appeared to be COM-rich. Moreover, Bianchi et al. (2020)

conducted a chemical survey of the L1551–IRS5 binary system and found that the brighter (1.3 mm) component (N) dominates the COM emission. For the ALMASOP YSO sample, observations with improved sensitivities will verify the existing but undiscovered hot-corino signatures in the YSOs with low envelope masses (marked the navy dots in Figure 3).

5.2. Complications

While this study suggests that the hot-corino signature commonly originates from the warm envelope, there are complications to this scenario regarding the presence of COMs and their detection in protostellar objects. For example, there may be temporal variations in the total luminosity and consequently the level of heating due to episodic accretion events, such as those seen in FU Ori objects. The extent of the warm region and equivalently the location of the snowline will therefore move outwards as a result of the outburst, as have been shown by literature such as van ’t Hoff et al. (2018) and Lee et al. (2019b). In addition, the radiation emitted from the central protostar may not be the only heating source in a protostellar system. Tabone et al. (2017) speculated that a different heating mechanism due to the accretion shocks might explain the presence of disk-origin COM emission near the centrifugal barrier of the Class 0 protostar HH–212 (Lee et al. 2017, 2019a). A similar mechanism was later suggested by Oya & Yamamoto (2020) based on the radial profile of the rotational temperature in H₂CS in IRAS 16293–2422 A. Recently, this localized heating mechanism was further supported by the ring-like elevated warm structure in the Class 0 protostar B335 (Okoda et al. 2022).

Furthermore, other mechanisms may also contribute to the presence of gaseous COMs in protostellar systems. These mechanisms include outflow shocks, where energetic outflows result in shock-induced desorption of COMs (Vastel et al. 2022), and reactive desorption, where the penetration of photons into the cavity leads to the photodissociation of icy COMs and the subsequent recombination of their photoproducts (Drozdovskaya et al. 2015). These mechanisms play a significant role in shaping the chemistry in protostellar systems and should be considered when studying the distribution and composition of COMs in YSO environments.

We also note that, in addition to the limitation due to observational sensitivity, other factors may affect the detectability of COM emission. Dust continuum opacity, for instance, could be one possible reason for a non-detection. Sahu et al. (2019) observed the protostellar binary system IRAS 4A1 and 4A2 and suggested that the absence of COM emission in IRAS 4A1 could be due to an optically thick circumstellar disk and/or different layers

of a temperature-stratified and dense envelope, which veils the COM emission and in fact results in COM absorption signatures. This hypothesis was subsequently supported by De Simone et al. (2020) through observations at longer, centimeter wavelengths at which the dust continuum opacity becomes optically thin. Similar effects may occur in SVS13–A binary system, as suggested by (Bianchi et al. 2022).

Finally, the non-detection of gaseous COMs may simply be due to a lack of COM emission in protostar cores. Oya et al. (2019) found that Elias 29, a Class I protostar, is (likely) poor in COMs as the desorbed COMs might have been destroyed by the proton transfer reactions. Alternatively, there may be chemical diversity between protostellar cores by nature. For example, Sakai et al. (2008) showed that the protostellar core in the low-mass star-forming region L1527 is rich in carbon-chain molecules but shows a lack of saturated COMs typically found in hot corinos. The authors introduced the concept of “warm-carbon-chain chemistry (WCCC)” to explain such chemical composition in the protostellar system. However, there are sources, (e.g., L483, Oya et al. 2017) exhibiting signatures of both hot-corino and WCCC simultaneously. It thus remains uncertain whether the sources subjected to WCCC indeed lack in gaseous saturated COMs.

5.3. Implications for Astrochemistry in Cores and Disks

Complex organic species, such as CH_3OH , previously residing on icy grain mantles, desorb into the gas phase as gas and grains migrate from the outer colder region into the warmer inner region of the infalling envelope. This process can be most naturally ubiquitous in embedded YSOs, as proposed by Ceccarelli (2004). The detection of hot-corino signatures, as entailed by our analysis, is dictated by the total amount of COMs, which is related to the size and density of the inner warm region in the infalling envelope and, equivalently, the luminosity and evolution stage of the YSO. The gaseous COMs (CH_3OH specifically in this study) seen in the warm inner infalling envelope may reflect the “fresh” ice composition in grain mantles, perhaps more closely than seen in massive hot molecular cores where the chemistry suffers additional alteration due to harsher UV radiation from the central massive YSOs (e.g., Olguin et al. 2022). The connection of the hot-corino signature to the chemistry in the later developed protoplanetary disks may depend on whether the COMs will get dispersed (Ferreira et al. 2006), destroyed in the gas phase (Charnley et al. 1992; Millar & Hatchell 1998; Nomura et al. 2009; Yoneda et al. 2016), or eventually settle within the disk. The inheritance nature of COMs in protoplanetary disks, as hinted by Yoneda et al. (2016), may depend on the location within the disk and the COM species. COMs seen in later stages of protoplanetary disks

are sometimes interpreted as of thermal desorption origin (van’t Hoff et al. 2020; Booth et al. 2021; van der Marel et al. 2021). In case their abundances are indicative of being inherited from the prestellar stage, the icy mantles are likely preserved with the dust grains accreted onto the outer and colder disk, as also discussed by Hincelin et al. (2013). The ice mantles then sublimated when dust grains migrate into the inner disk inside the snowline, or the snowline gets pushed outwards from a luminosity burst event (Lee et al. 2019b). Minor bodies in the solar system exhibiting inheritance of ISM chemistry may have a similar accretion and thermal history.

6. CONCLUSIONS

1. We carry out SED fitting analysis for the Class 0/I protostars previously observed by the ALMASOP project and report the distributions of the modeled YSO physical parameters. The differentiation in the YSO model parameters among the sources with and without hot-corino signatures implies a link between the detection of the hot-corino signature and the envelope density profile for YSOs with similar luminosity. Our modeling results suggest that the sources with hot-corino signatures have high luminosities, envelope densities, and consequently high warm envelope mass.
2. We further carry out simulations of the methanol moment-0 integrated intensity images and compared them with the ALMASOP observations. The “envelope+disk” models produce the synthetic CH_3OH images matching with the ALMASOP observations significantly better than the “disk” models.
3. Our study favors the hypothesis that the origin of the detected hot-corino signature is commonly the warm region within the protostellar envelope. Under this scenario, the detectability of a hot corino depends on the warm envelope mass, determined by the warm region size and the envelope density profile. The former is governed by the source luminosity and is additionally affected by the whole protostellar structure, such as the disk and cavity. The latter is related to the YSO evolutionary stage.
4. The presence of gaseous COMs in the warm inner envelopes can be most naturally ubiquitous in embedded YSOs. The gaseous COMs seen in the warm inner envelope in sources with hot-corino signature may reflect the “fresh” ice composition in grain mantles.

ACKNOWLEDGMENTS

This paper makes use of the following ALMA data: ADS/JAO.ALMA#2018.1.00302.S. ALMA is a partnership of ESO (representing its member states), NSF (USA), and NINS (Japan), together with NRC (Canada), MOST and ASIAA (Taiwan), and KASI (Republic of Korea), in cooperation with the Republic of Chile. The Joint ALMA Observatory is operated by ESO, AUI/NRAO, and NAOJ. SYH and SYL acknowledge support from the Ministry of Science and Technology (MoST) with grants 110-2112-M-001-056- and 111-2112-M-001-042-. D.S. acknowledges the support from Ramanujan Fellowship (SERB) and PRL, India. This work has been supported by the National Key R&D Program of China (No. 2022YFA1603100). Tie Liu acknowledges the supports by National Natural Science Foundation of China (NSFC) through grants No.12122307 and No.12073061, the international partnership program of Chinese Academy of Sciences through grant No.114231KYSB20200009, Shanghai Pujiang Program 20PJ1415500 and the science research grants from the China Manned Space Project with no. CMS-CSST-2021-B06 MJ acknowledges support from the Academy of Finland grant No. 348342. The work of MGR is supported by NOIRLab, which is managed by the Association of Universities for Research in Astronomy (AURA) under a cooperative agreement with the National Science Foundation. LB gratefully acknowledges support by the ANID BASAL project FB210003. Y.-L. Y. acknowledges support from Grant-in-Aid from the Ministry of Education, Culture, Sports, Science, and Technology of Japan (JP 22K20389, JP 20H05845, JP 20H05844), and a pioneering project in RIKEN (Evolution of Matter in the Universe). This research made use of Astropy,⁴ a community-developed core Python package for Astronomy (Astropy Collaboration et al. 2013; Price-Whelan et al. 2018). K.T. was supported by JSPS KAKENHI (Grant Number JP20H05645). DJ is supported by NRC Canada and by an NSERC Discovery Grant. PS was partially supported by a Grant-in-Aid for Scientific Research (KAKENHI Number JP22H01271 and JP23H01221) of JSPS.

Software: astropy (Astropy Collaboration et al. 2013; Price-Whelan et al. 2018), CASA (McMullin et al. 2007), HO-CHUNK (Whitney et al. 2003b) SED Fitter (Robitaille et al. 2006, 2007) SPARX

Table A1. The information of the observation for SED.

Observatory	WISE	<i>Spitzer</i>	AKARI PSC	<i>Spitzer</i>	<i>Herschel</i>	APEX	ALMA
Filter or Band	W1, W2, W3, W4	IRAC	IRC S9W, L18W	MIPS	PACS	SABOCA, LABOCA	Band 6
Wavelength (μm)	3.4, 4.6, 12, 22	3.6, 4.5, 5.8,	9, 18	24	70, 100, 160	350, 870	1300
Aperture radius	6''1, 6''4, 6''5, 12''0	2''4	5''5, 5''7	6''0	9''6, 9''6, 12''8	3''7, 8''5	$\sim 0''.45$

NOTE— The SED flux data points were collected from [Dutta et al. \(2020\)](#).

References— WISE: [Wright et al. \(2010\)](#) *Spitzer*: [Werner et al. \(2004\)](#); IRAC: [Fazio et al. \(2004\)](#); MIPS: [Rieke et al. \(2004\)](#); AKARI PSC: [Ishihara et al. \(2010\)](#); *Herschel*: [Pilbratt et al. \(2010\)](#); PACS: [Poglitsch et al. \(2010\)](#); APEX: [Güsten et al. \(2006\)](#); SABOCA: [Siringo et al. \(2010\)](#); LABOCA: [Siringo et al. \(2009\)](#);

APPENDIX

A. SED ANALYSIS

All the photometric data points we use for the SED fitting can be found in Table 6 of [Dutta et al. \(2020\)](#). Also, Table C1 in [Hsu et al. \(2022\)](#) shows the wavelength, the aperture radius, the instrument, and the observatory for each SED photometric data point. The aperture is the field of observation for extracting the flux. The references include UKIRT/UKIDSS ([Lawrence et al. 2007](#)), WISE ([Wright et al. 2010](#)), *Spitzer* ([Werner et al. 2004](#)), IRAC ([Fazio et al. 2004](#)), MIPS ([Rieke et al. 2004](#)), AKARI PSC ([Ishihara et al. 2010](#)), AKARI BSC ([Yamamura 2010](#)), *Herschel* ([Pilbratt et al. 2010](#)), PACS ([Poglitsch et al. 2010](#)), APEX ([Güsten et al. 2006](#)), SABOCA ([Siringo et al. 2010](#)), LABOCA ([Siringo et al. 2009](#)), and JCMT/SCUBA2 ([Di Francesco et al. 2008](#)).

Figure A1 shows the SED data points and the nine best-fit YSO models in the R06 grid of our sample. Table A1 shows representative wavelengths and apertures of the archival SED data points. Table A2 shows the names of the top nine best-fit models in the R06 grid. Table A3 shows the weighted average and standard deviation of the YSO parameters. Figure A2 shows the distributions of the YSO parameters for the ALMASOP sample as well as those in the R06 grid. Table A4 shows the YSO model parameters for the SPARX simulation.

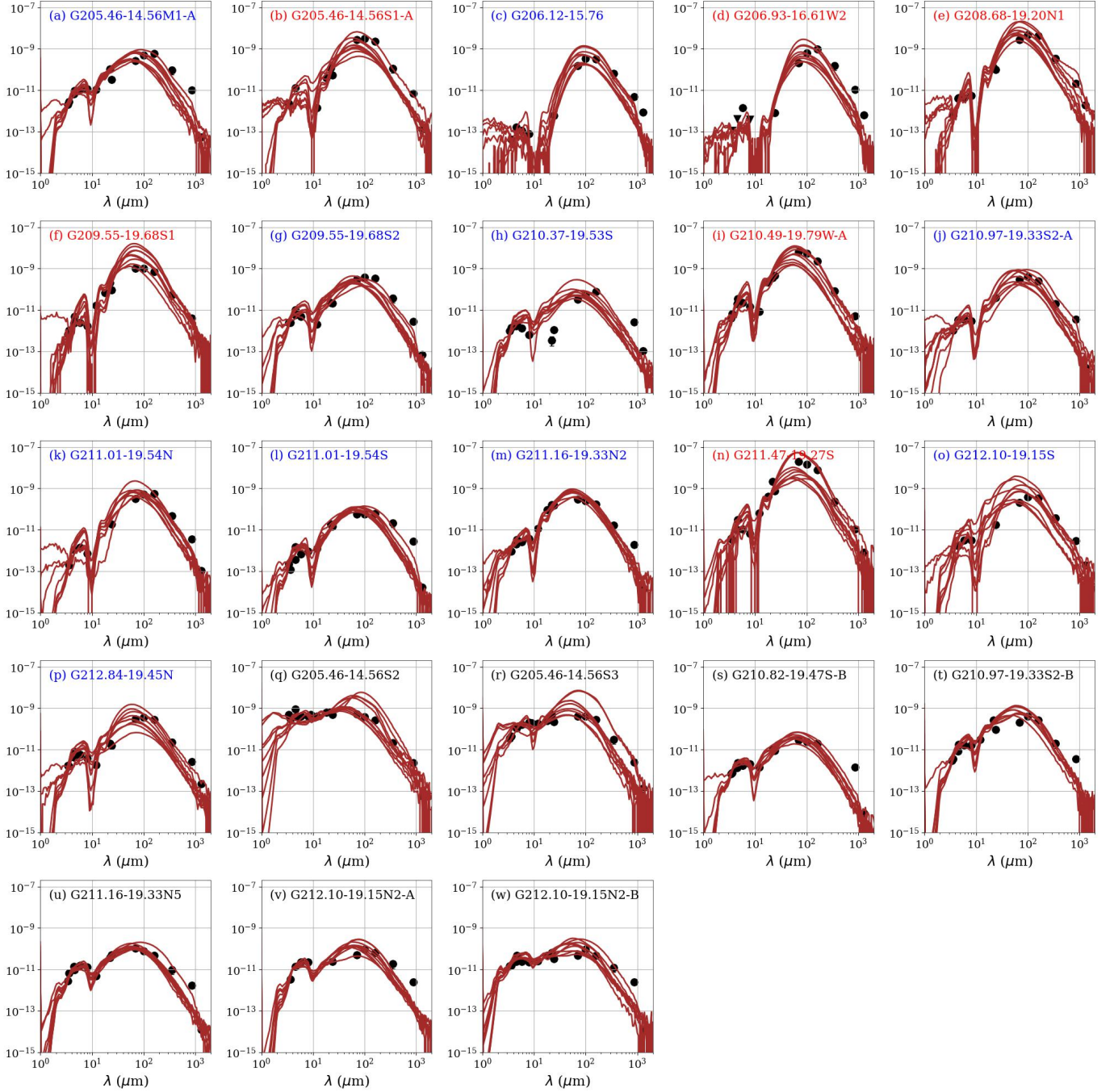


Figure A1. The SEDs of the input data points and the nine best-fit YSO models of the sample. The triangle represents the upper limit of the observation. The source names of the Class 0 YSOs with hot-corino signatures, Class 0 YSOs without hot-corino signatures, and Class I YSOs are labeled in red, blue, and black, respectively. The uncertainties of the measurements are shown by the error bars around each data point. In most cases, though, the uncertainties are too small to be visible.

Table A2. YSO model names in R06 grid.

Model name in R06 grid	N_{data}	A_V	χ^2/N_{data}
G205.46-14.56M1-A (HOPS-317)			
3006805_10	15	23.135	78.583
3006939_10	15	23.516	82.092
3012536_10	15	19.237	83.349
3005566_10	15	22.333	85.900
3009879_10	15	23.034	88.395
3005643_10	15	22.625	90.105
3014595_9	15	21.229	90.247
3001845_8	15	27.964	94.457
3013127_10	15	17.995	95.709
G205.46-14.56S1-A (HOPS-358)			
3014523_9	12	3.613	208.878
3011935_8	12	5.935	221.710
3002461_10	12	23.007	245.541
3009148_10	12	30.000	248.360
3010028_7	12	0.000	255.945
3005113_5	12	1.461	256.502
3010028_6	12	0.000	262.822
3008121_7	12	2.148	266.323
3008863_9	12	5.414	270.784
G206.12-15.76 (HOPS-400)			
3017827_6	11	20.574	229.908
3019250_6	11	0.000	234.913
3009181_5	11	0.000	246.033
3009181_4	11	0.000	246.353
3019843_5	11	0.000	248.696
3018837_6	11	5.321	252.159
3006939_6	11	0.000	253.697
3006939_8	11	15.450	265.850
3019250_7	11	6.619	267.953
G206.93-16.61W2 (HOPS-399)			
3002461_9	8	15.752	252.666
3005362_8	8	0.000	284.334
3019843_5	8	0.000	320.805
3012334_9	8	30.000	329.824
3009148_8	8	0.000	330.642
3009181_5	8	0.000	331.898
3019250_8	8	16.745	367.835
3009879_7	8	30.000	368.282

Table A2 *continued***Table A2** (*continued*)

Model name in R06 grid	N_{data}	A_V	χ^2/N_{data}
3010733_8	8	0.000	374.607
G208.68-19.20N1 (HOPS-87)			
3016258_9	13	8.095	54.252
3014529_9	13	5.296	59.694
3006540_8	13	2.223	63.229
3005436_8	13	6.909	66.938
3005775_8	13	9.710	76.891
3002402_8	13	0.169	78.863
3014904_7	13	5.035	82.825
3010556_9	13	5.908	89.031
3008121_8	13	8.064	103.819
G209.55-19.68S1 (HOPS-11)			
3011928_4	16	10.960	122.152
3011928_5	16	11.881	130.989
3004222_3	16	7.772	145.699
3009693_2	16	1.848	157.422
3009777_4	16	10.125	170.472
3008378_4	16	11.437	171.059
3005928_4	16	11.379	172.466
3009693_3	16	1.974	176.950
3002996_5	16	11.828	177.034
G209.55-19.68S2 (HOPS-10)			
3009892_9	14	16.250	44.997
3009892_10	14	27.630	77.512
3007523_8	14	11.352	93.191
3004378_9	14	17.203	113.368
3014404_7	14	14.263	117.119
3014404_6	14	8.636	122.589
3012738_9	14	14.629	122.823
3017475_10	14	27.317	134.346
3014404_8	14	19.390	139.609
G210.37-19.53S (HOPS-164)			
3016014_8	13	0.000	225.875
3016088_7	13	0.000	339.335
3017966_8	13	0.000	342.525
3016014_9	13	18.473	356.746
3016405_7	13	0.585	368.181
3016088_8	13	8.136	369.887
3001740_7	13	0.000	428.333
3017966_9	13	16.040	431.541
3016405_6	13	0.000	436.016

Table A2 *continued*

Table A2 (*continued*)

Model name in R06 grid	N_{data}	A_V	χ^2/N_{data}
G210.49-19.79W-A (HOPS-168)			
3001830_7	16	11.145	153.828
3011394_9	16	16.180	172.130
3011804_9	16	0.000	175.677
3018997_7	16	10.516	180.504
3009709_7	16	2.878	186.461
3018997_8	16	21.418	191.588
3017681_9	16	7.739	196.365
3004153_9	16	30.000	199.019
3004153_8	16	23.076	204.329
G210.97-19.33S2-A (HOPS-377)			
3013814_8	11	5.853	20.312
3000179_7	11	5.800	23.044
3006477_5	11	2.726	24.096
3014595_8	11	8.858	24.317
3016693_10	11	30.000	24.697
3015398_8	11	4.719	27.010
3012983_7	11	4.184	29.173
3006477_6	11	8.451	29.361
3010511_9	11	0.000	29.877
G211.01-19.54N (HOPS-153)			
3014886_8	11	0.000	96.148
3013814_8	11	21.044	106.305
3009879_8	11	9.614	107.687
3013407_7	11	0.000	111.200
3007761_6	11	10.438	119.725
3014595_7	11	9.052	135.005
3009785_5	11	19.017	140.722
3007761_5	11	7.335	141.676
3001459_5	11	18.543	144.308
G211.01-19.54S (HOPS-152)			
3016405_10	15	29.014	85.718
3016405_9	15	22.442	89.371
3019917_5	15	26.139	98.265
3019266_9	15	14.416	101.512
3016405_8	15	15.040	102.875
3016436_6	15	19.492	103.737
3000014_3	15	19.884	104.242
3016933_4	15	11.905	105.633
3016436_7	15	25.796	106.186
G211.16-19.33N2 (HOPS-133)			

Table A2 *continued***Table A2** (*continued*)

Model name in R06 grid	N_{data}	A_V	χ^2/N_{data}
3013740_2	16	15.108	34.785
3014342_4	16	13.264	37.383
3013740_1	16	13.474	45.458
3011658_7	16	15.492	45.862
3019064_2	16	15.789	46.484
3008896_2	16	14.151	47.783
3004836_2	16	18.687	48.488
3014342_3	16	11.539	49.737
3012810_2	16	15.469	50.911
G211.47-19.27S (HOPS-288)			
3013227_3	16	2.480	527.642
3001398_5	16	9.019	556.939
3001398_4	16	7.123	564.907
3003853_5	16	2.751	582.541
3003853_6	16	5.320	588.719
3002254_7	16	0.920	597.693
3001398_6	16	11.424	600.840
3015663_7	16	2.601	606.336
3018117_3	16	6.943	612.036
G212.10-19.15S (HOPS-247)			
3005643_6	10	1.048	235.502
3003151_4	10	30.000	261.213
3017475_5	10	16.717	289.215
3004609_5	10	30.000	306.891
3009907_4	10	7.759	389.509
3003151_3	10	25.165	408.486
3004356_6	10	6.092	415.491
3014900_1	10	29.053	421.456
3007124_3	10	0.000	453.359
G212.84-19.45N (HOPS-224)			
3019250_9	15	0.000	248.868
3003541_9	15	0.461	335.326
3008016_10	15	27.766	358.632
3019250_10	15	24.251	365.757
3008016_8	15	25.439	372.744
3005566_9	15	4.101	394.948
3002333_9	15	0.000	411.531
3020156_8	15	0.000	424.541
3010316_10	15	26.172	435.676
G205.46-14.56S2 (HOPS-385)			
3016440_10	17	4.909	75.117

Table A2 *continued*

Table A2 (continued)

Model name in R06 grid	N_{data}	A_V	χ^2/N_{data}
3011896_6	17	8.022	96.039
3011896_5	17	6.546	105.905
3011528_9	17	7.285	115.080
3012552_10	17	2.238	121.903
3009117_10	17	16.597	122.467
3011528_10	17	4.301	123.620
3016440_9	17	5.757	129.535
3011528_7	17	9.356	131.427
G205.46-14.56S3 (HOPS-315)			
3008309_7	17	13.150	226.404
3011896_9	17	24.156	238.779
3008309_6	17	10.996	246.721
3019313_9	17	12.236	252.863
3005398_10	17	13.213	255.839
3005398_9	17	10.780	274.785
3012951_10	17	18.821	284.815
3019313_8	17	11.665	285.554
3012951_8	17	20.191	305.153
G210.82-19.47S-B (HOPS-156)			
3010723_9	14	21.197	35.742
3010723_10	14	20.958	35.882
3010723_8	14	20.030	37.207
3010723_7	14	17.999	40.553
3018870_8	14	20.266	42.793
3018870_9	14	20.773	43.170
3019589_3	14	8.568	45.000
3010723_6	14	15.452	45.383
3009216_6	14	9.514	46.723
G210.97-19.33S2-B (HOPS-144)			
3013740_5	15	12.112	74.878
3011479_7	15	25.758	79.555
3004010_4	15	13.951	83.067
3013740_4	15	9.617	83.537
3011479_6	15	24.852	83.943
3019417_3	15	14.649	84.484
3011479_8	15	26.378	84.711
3013740_7	15	17.472	85.651
3011479_5	15	23.674	85.834
G211.16-19.33N5 (HOPS-135)			
3014344_7	15	18.646	29.519
3014344_6	15	17.417	31.366

Table A2 continued**Table A2** (continued)

Model name in R06 grid	N_{data}	A_V	χ^2/N_{data}
3008016_9	15	20.244	31.843
3008016_10	15	21.310	32.069
3014344_8	15	19.848	32.703
3014344_5	15	16.185	34.242
3008016_8	15	18.865	34.478
3014344_9	15	21.111	34.554
3014344_4	15	14.497	36.609
G212.10-19.15N2-A (HOPS-263)			
3007105_9	11	21.206	24.748
3007105_10	11	21.678	26.044
3013344_6	11	25.332	28.741
3013344_7	11	28.806	30.606
3013909_10	11	24.551	31.183
3005143_10	11	25.532	33.147
3013344_5	11	20.258	34.300
3013909_9	11	22.049	34.627
3007105_8	11	16.563	36.950
G212.10-19.15N2-B (HOPS-262)			
3002125_6	16	9.734	67.505
3002125_7	16	11.270	68.280
3009559_7	16	10.327	69.411
3013344_6	16	11.133	69.458
3009559_8	16	12.033	70.556
3013344_7	16	14.650	71.304
3009783_7	16	9.412	71.585
3002125_8	16	12.553	71.788
3011716_8	16	14.274	72.791

NOTE—For each source, nine best-fit YSO models are presented in the order of the goodness of the model. N_{data} is the number of photometric measurement for fitting. A_V is the additional extinction. χ^2 is the goodness of fitting defined by Robitaille et al. (2007) and shown in Equation 1. χ^2/N_{data} is the χ^2 -per-data point value defined by Robitaille et al. (2007), indicating the goodness of the fitting.

References—R06 grid: Robitaille et al. (2006)

Table A3. The weighted average and standard deviation of the YSO model parameters.

Source	L_{tot}	t_*	M_*	R_*	T_*	$R_{\text{inner}}^{\text{outer}}$	$R_{\text{disk}}^{\text{outer}}$	\dot{M}_{disk}	M_{disk}	$z_{\text{disk}}^{\text{scale}}$	B_{disk}	$R_{\text{env}}^{\text{outer}}$	\dot{M}_{env}	θ_{cav}	ρ_{cav}	ρ_{amb}	φ	
	(\log_{10})	yr	M_{\odot}	R_{\odot}	K	au	au	$M_{\odot} \text{ yr}^{-1}$	(\log_{10})	(\log_{10})	(\log_{10})	(\log_{10})	M_{\odot}	$^{\circ}$	g cm^{-3}	g cm^{-3}	$^{\circ}$	
	(\log_{10})	(\log_{10})	(\log_{10})	(\log_{10})	(\log_{10})	(\log_{10})	(\log_{10})	(\log_{10})	(\log_{10})	(\log_{10})	(\log_{10})	(\log_{10})	(\log_{10})	(\log_{10})	(\log_{10})	(\log_{10})	(\log_{10})	$^{\circ}$
G205.46-14.56M1-A	0.5±0.2	4.5±0.6	-0.4±0.2	0.6±0.1	3509±327	-0.1±0.8	1.5±0.4	-6.9±0.4	-2.2±0.4	0.8±0.1	1.08±0.04	3.5±0.3	4.2±0.2	20.3±6.8	-19.8±0.5	-21.9±0.2	22.0±7.8	
G205.46-14.56S1-A	1.2±0.3	4.0±0.4	-0.1±0.2	0.9±0.1	3940±175	-0.5±0.3	1.2±0.5	-6.6±0.8	-2.1±0.5	0.9±0.1	1.13±0.05	3.8±0.3	-3.9±0.2	12.7±3.4	-19.7±0.2	-21.4±0.3	39.6±15.1	
G206.12-15.76	0.5±0.2	4.3±0.3	-0.5±0.1	0.7±0.1	3421±230	-0.7±0.5	1.5±0.3	-6.8±0.5	-2.0±0.6	0.8±0.1	1.12±0.04	3.3±0.1	-3.9±0.2	18.5±1.9	-19.8±0.4	-21.8±0.2	57.2±7.6	
G206.93-16.61W2	0.6±0.2	4.2±0.4	-0.4±0.1	0.7±0.1	3548±214	-0.5±0.5	1.4±0.2	-6.8±0.6	-1.9±0.6	0.8±0.1	1.11±0.05	3.6±0.3	-3.9±0.2	15.2±1.9	-19.8±0.3	-21.8±0.2	44.6±11.2	
G208.68-19.20N1	1.6±0.1	3.9±0.3	0.0±0.2	1.0±0.1	4017±181	-0.2±0.4	1.1±0.3	-5.4±0.4	-1.1±0.3	0.9±0.1	1.09±0.05	3.6±0.1	-3.8±0.2	11.9±2.0	-19.7±0.3	-21.3±0.3	38.6±5.7	
G209.55-19.68S1	1.3±0.1	3.7±0.4	-0.2±0.2	0.9±0.1	3828±202	-0.3±0.2	0.9±0.4	-5.6±0.7	-1.7±0.3	0.8±0.1	1.13±0.07	3.5±0.3	-4.5±0.2	8.9±2.3	-19.5±0.2	-21.7±0.2	70.7±5.6	
G209.55-19.68S2	0.4±0.1	4.5±0.2	-0.4±0.1	0.6±0.0	3498±135	-0.9±0.1	1.7±0.2	-7.2±0.5	-2.0±0.5	0.8±0.0	1.08±0.05	3.7±0.1	-4.3±0.4	22.0±3.5	-19.7±0.3	-21.8±0.1	34.4±11.5	
G210.37-19.55S	-0.1±0.1	4.7±0.3	-0.8±0.1	0.5±0.1	2953±120	-0.9±0.7	1.6±0.1	-7.7±0.4	-2.1±0.1	0.8±0.1	1.10±0.06	3.2±0.1	-4.5±0.3	23.0±3.1	-19.9±0.2	-22.0±0.0	43.4±7.5	
G210.49-19.79W-A	1.6±0.1	4.6±0.5	0.3±0.1	1.1±0.1	4261±100	-0.4±0.0	1.4±0.3	-6.7±0.7	-1.5±0.7	0.9±0.1	1.07±0.07	4.2±0.3	-3.6±0.2	19.8±4.4	-19.9±0.5	-21.2±0.3	40.0±7.9	
G210.97-19.33S2-A	0.5±0.1	4.6±0.3	-0.4±0.1	0.6±0.0	3655±122	-0.6±0.7	1.7±0.2	-7.4±0.6	-2.3±0.5	0.8±0.1	1.12±0.06	3.4±0.3	-4.2±0.3	21.9±6.1	-19.9±0.3	-21.7±0.1	43.6±12.6	
G211.01-19.54N	0.7±0.2	4.4±0.5	-0.3±0.1	0.7±0.1	3665±165	-0.4±0.5	1.5±0.2	-6.7±0.6	-1.7±0.3	0.8±0.1	1.10±0.05	3.5±0.3	-4.2±0.3	18.4±4.5	-19.9±0.2	-21.8±0.2	51.0±9.1	
G211.01-19.54S	-0.1±0.2	4.7±0.5	-0.8±0.1	0.5±0.1	2994±205	0.3±0.7	1.6±0.2	-7.2±0.4	-2.2±0.4	0.8±0.1	1.08±0.06	3.2±0.1	-5.2±0.2	19.8±6.7	-20.1±0.4	-22.0±0.1	47.6±18.5	
G211.16-19.33N2	0.8±0.1	4.2±0.6	-0.3±0.1	0.7±0.1	3664±197	-0.3±0.9	1.3±0.4	-6.6±0.5	-2.5±0.7	0.8±0.1	1.09±0.06	3.6±0.1	-5.2±0.1	12.3±3.1	-19.6±0.4	-21.8±0.2	76.4±10.5	
G211.47-19.27S	2.0±0.1	4.0±0.3	0.3±0.1	1.2±0.1	4221±57	0.1±0.4	1.2±0.2	-5.2±0.6	-1.2±0.3	0.8±0.1	1.09±0.07	3.5±0.3	-3.9±0.2	11.4±2.6	-19.6±0.2	-21.2±0.3	62.4±9.4	
G212.10-19.15S	0.8±0.3	4.7±0.5	-0.2±0.2	0.7±0.1	3871±206	0.2±0.8	1.6±0.4	-7.0±0.7	-1.7±0.3	0.9±0.1	1.08±0.06	3.4±0.3	-4.4±0.3	26.7±6.8	-20.0±0.3	-21.6±0.1	67.3±8.9	
G212.84-19.45N	0.3±0.1	4.5±0.4	-0.6±0.1	0.6±0.1	3198±216	-1.0±0.2	1.6±0.3	-6.9±0.7	-1.8±0.2	0.8±0.1	1.08±0.06	3.4±0.1	-4.6±0.5	16.3±1.4	-20.1±0.3	-21.9±0.1	29.5±8.5	
G205.46-14.56S2	1.7±0.2	5.5±0.2	0.6±0.1	1.0±0.0	5000±392	0.4±0.6	1.8±0.1	-7.0±0.7	-1.5±0.6	0.8±0.1	1.12±0.07	4.1±0.2	-5.5±0.5	39.3±8.3	-20.3±0.1	-20.9±0.3	34.0±17.4	
G205.46-14.56S3	1.4±0.2	5.1±0.6	0.2±0.3	0.9±0.1	4467±479	0.0±0.5	1.8±0.2	-6.5±0.6	-1.3±0.3	0.9±0.1	1.06±0.03	3.9±0.1	-5.2±0.8	27.3±6.1	-20.3±0.5	-21.3±0.3	35.9±12.4	
G210.82-19.47S-B	-0.3±0.0	4.9±0.3	-0.9±0.1	0.4±0.0	2907±130	0.4±0.9	1.6±0.1	-7.9±0.2	-2.4±0.1	0.7±0.0	1.15±0.06	3.3±0.1	-5.3±0.2	29.2±10.4	-20.0±0.2	-22.0±0.0	43.6±16.0	
G210.97-19.33S2-B	0.9±0.1	4.3±0.1	-0.2±0.1	0.8±0.0	3839±73	0.1±1.0	1.5±0.1	-6.8±0.3	-2.3±0.2	0.9±0.1	1.04±0.03	3.8±0.2	-5.3±0.1	14.4±5.1	-19.7±0.1	-21.6±0.1	59.8±10.6	
G211.16-19.33N5	0.2±0.0	4.6±0.2	-0.6±0.1	0.6±0.0	3265±109	-1.0±0.1	1.8±0.1	-7.4±0.3	-1.8±0.2	0.8±0.0	1.12±0.01	3.5±0.0	-5.7±0.1	12.9±1.5	-20.0±0.3	-22.0±0.0	44.6±15.4	
G212.10-19.15N2-A	0.2±0.2	4.8±0.3	-0.6±0.2	0.5±0.0	3277±287	-0.9±0.3	1.6±0.2	-6.6±0.2	-2.0±0.3	0.9±0.1	1.15±0.06	3.5±0.1	-4.9±0.4	31.7±7.8	-20.1±0.3	-21.9±0.1	36.1±16.1	
G212.10-19.15N2-B	0.3±0.1	4.4±0.5	-0.5±0.1	0.6±0.1	3318±211	-0.9±0.3	1.6±0.3	-7.1±0.6	-1.9±0.3	0.9±0.1	1.18±0.01	3.5±0.1	-5.4±0.5	22.6±10.9	-19.9±0.4	-21.8±0.1	48.5±5.6	

NOTE—The L_{tot} is the total luminosity. The t_* is the evolutionary age. The M_* , R_* and T_* are the mass, the radius and the temperature of central protostar, respectively. The M_{disk} is the total mass of disk. The \dot{M}_{disk} and \dot{M}_{env} are the mass accretion rate of disk and the in-fall rate of envelope, respectively. The R_{inner} is the inner radius of both envelope and disk. The $R_{\text{disk}}^{\text{outer}}$ and $R_{\text{env}}^{\text{outer}}$ are respectively the outer radius of disk and envelope. The θ_{cav} is the opening angle of cavity. The ρ_{cav} and the ρ_{amb} are respectively cavity density and ambient density. The φ is the viewing angle.

Table A4. The YSO model parameters for SPARX simulation.

		G208N1	G210WA	G211S
M_*	M_\odot	1.586	2.446	1.939
R_*	R_\odot	10.8	12.7	16.2
T_*	K	4202	4357	4131
R^{inner}	au	0.38	0.48	1.87
$R_{\text{env}}^{\text{outer}}$	au	2219	3507	3108
$R_{\text{disk}}^{\text{outer}} = R_C$	au	16.0	34.2	8.5
\dot{M}_{env}	$M_\odot \text{ yr}^{-1}$	3.1×10^{-4}	3.0×10^{-4}	9.7×10^{-5}
\dot{M}_{disk}	$M_\odot \text{ yr}^{-1}$	2.1×10^{-6}	3.6×10^{-7}	5.6×10^{-6}
M_{disk}	M_\odot	0.139	0.080	0.027
$z_{\text{disk}}^{\text{scale}}$		0.87	0.73	1.00
B_{disk}		1.087	1.098	1.216
θ_{cav}	$^\circ$	13.3	30.4	7.1
φ	$^\circ$	31.8	49.5	75.5
ρ_{cav}	g cm^{-3}	1.2×10^{-20}	4.8×10^{-21}	2.8×10^{-20}
ρ_{amb}	g cm^{-3}	9.3×10^{-22}	1.2×10^{-21}	4.2×10^{-22}

NOTE— See Table A3 for the meaning of the symbols.

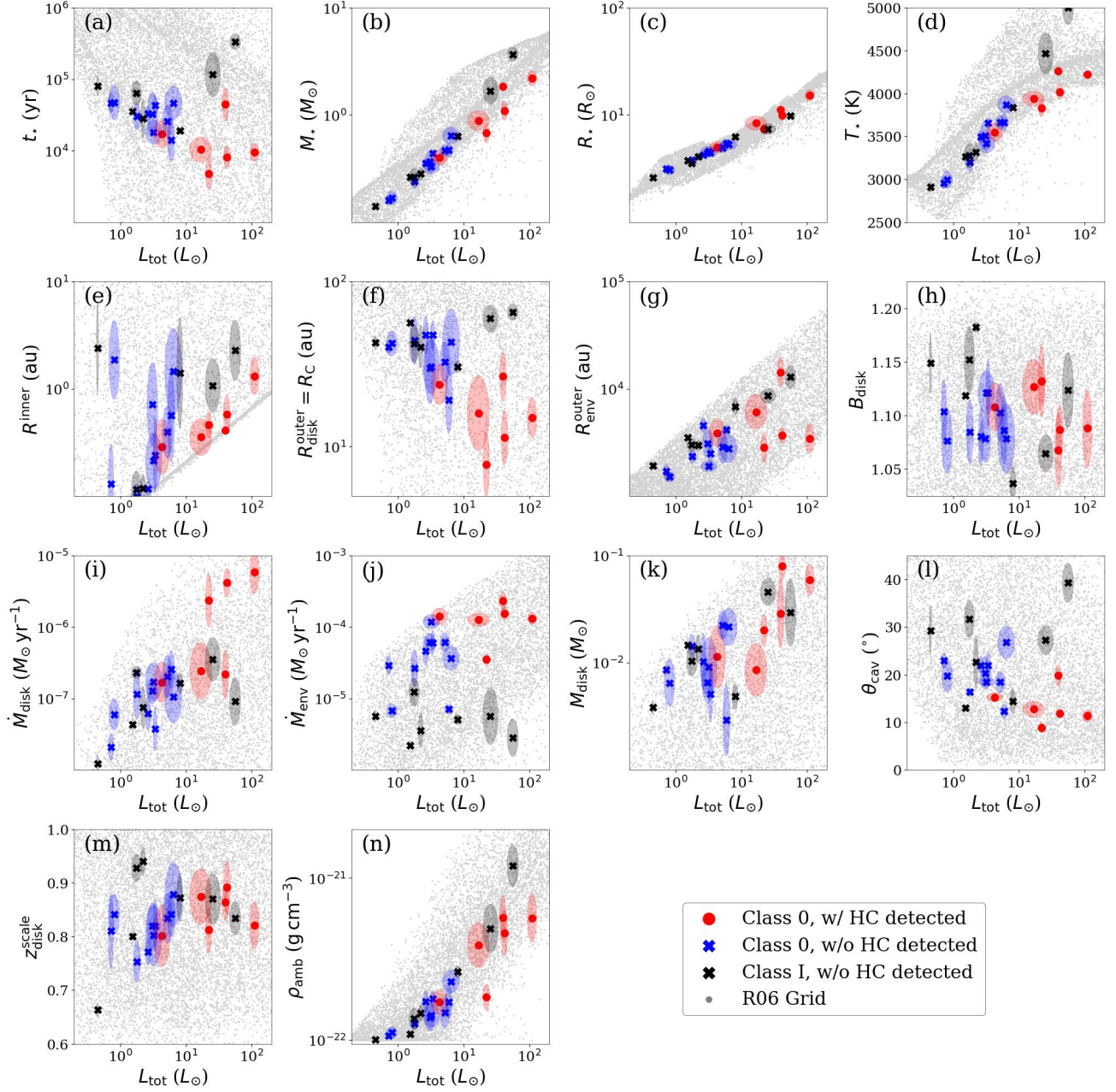


Figure A2. Weighted average and standard deviation of each YSO model parameter versus total luminosity (L_{tot}). The x-axes of all sub-figures are total luminosities (L_{tot}). The text of each sub-figure shows the label of the y-axis. The t_* is the evolutionary age of the protostellar system. The M_* , R_* , and T_* are the mass, the radius, and the temperature of the central protostar, respectively. The R^{inner} is the inner radius of both envelope and disk. The $R_{\text{disk}}^{\text{outer}}$ and $R_{\text{env}}^{\text{outer}}$ are the outer radius of the disk and envelope, respectively. The B_{disk} is the disk-flaring factor. The \dot{M}_{disk} and \dot{M}_{env} are the disk accretion rate and the envelope infall rate, respectively. The M_{disk} is the total mass of the disk. The θ_{cav} is the opening angle of the cavity. The $z_{\text{disk}}^{\text{scale}}$ is the factor to the disk scale height under hydrostatic equilibrium. The ρ_{amb} is the ambient density. The $\rho_{\text{env},C}$ is the characteristic envelope density. The red circles represent the sources with hot-corino signature Hsu et al. (2020, 2022). The blue and black crosses represent the Class 0 and Class I protostars where the hot corinos are not detected, respectively. The grey dots represent all the YSO models in the R06 grid.

B. METHANOL EMISSION SIMULATION

Table B1 shows the SPARX simulation results of the nine best-matching YSO models.

REFERENCES

- Arce, H. G., & Sargent, A. I. 2006, *ApJ*, 646, 1070, doi: [10.1086/505104](https://doi.org/10.1086/505104)
- Artur de la Villarmois, E., Kristensen, L. E., Jørgensen, J. K., et al. 2018, *A&A*, 614, A26, doi: [10.1051/0004-6361/201731603](https://doi.org/10.1051/0004-6361/201731603)
- Astropy Collaboration, Robitaille, T. P., Tollerud, E. J., et al. 2013, *A&A*, 558, A33, doi: [10.1051/0004-6361/201322068](https://doi.org/10.1051/0004-6361/201322068)
- Belloche, A., Maury, A. J., Maret, S., et al. 2020, *A&A*, 635, A198, doi: [10.1051/0004-6361/201937352](https://doi.org/10.1051/0004-6361/201937352)
- Bergner, J. B., Martín-Doménech, R., Öberg, K. I., et al. 2019, *ACS Earth and Space Chemistry*, 3, 1564, doi: [10.1021/acsearthspacechem.9b00059](https://doi.org/10.1021/acsearthspacechem.9b00059)
- Bergner, J. B., Öberg, K. I., Bergin, E. A., et al. 2020, *ApJ*, 898, 97, doi: [10.3847/1538-4357/ab9e71](https://doi.org/10.3847/1538-4357/ab9e71)
- Bianchi, E., López-Sepulcre, A., Ceccarelli, C., et al. 2022, *ApJ*, 928, L3, doi: [10.3847/2041-8213/ac5a56](https://doi.org/10.3847/2041-8213/ac5a56)
- Bianchi, E., Chandler, C. J., Ceccarelli, C., et al. 2020, *MNRAS*, 498, L87, doi: [10.1093/mnras/slaa130](https://doi.org/10.1093/mnras/slaa130)
- Boogert, A. C. A., Gerakines, P. A., & Whittet, D. C. B. 2015, *ARA&A*, 53, 541, doi: [10.1146/annurev-astro-082214-122348](https://doi.org/10.1146/annurev-astro-082214-122348)
- Booth, A. S., Walsh, C., Terwisscha van Scheltinga, J., et al. 2021, *NatAs*, 5, 684, doi: [10.1038/s41550-021-01352-w](https://doi.org/10.1038/s41550-021-01352-w)
- Bouvier, M., Ceccarelli, C., López-Sepulcre, A., et al. 2022, *ApJ*, 929, 10, doi: [10.3847/1538-4357/ac5904](https://doi.org/10.3847/1538-4357/ac5904)
- Brunken, N. G. C., Booth, A. S., Leemker, M., et al. 2022, *A&A*, 659, A29, doi: [10.1051/0004-6361/202142981](https://doi.org/10.1051/0004-6361/202142981)
- Cassen, P., & Moosman, A. 1981, *Icarus*, 48, 353, doi: [10.1016/0019-1035\(81\)90051-8](https://doi.org/10.1016/0019-1035(81)90051-8)
- Cazaux, S., Tielens, A. G. G. M., Ceccarelli, C., et al. 2003, *ApJ*, 593, L51, doi: [10.1086/378038](https://doi.org/10.1086/378038)
- Ceccarelli, C. 2004, in *Star Formation in the Interstellar Medium: In Honor of David Hollenbach, Chris McKee and Frank Shu*, ASP Conference Proceeding, ed. D. Johnstone, F. Adams, D. Lin, D. Neufeld, & E. Ostriker, Vol. 323, San Francisco, Astronomical Society of the Pacific (ASP Conference Proceedings)
- Charnley, S. B., Tielens, A. G. G. M., & Millar, T. J. 1992, *ApJ*, 399, L71, doi: [10.1086/186609](https://doi.org/10.1086/186609)
- Codella, C., Ceccarelli, C., Cabrit, S., et al. 2016, *A&A*, 586, L3, doi: [10.1051/0004-6361/201527424](https://doi.org/10.1051/0004-6361/201527424)
- De Simone, M., Ceccarelli, C., Codella, C., et al. 2020, *ApJ*, 896, L3, doi: [10.3847/2041-8213/ab8d41](https://doi.org/10.3847/2041-8213/ab8d41)
- Di Francesco, J., Johnstone, D., Kirk, H., MacKenzie, T., & Ledwosinska, E. 2008, *ApJS*, 175, 277, doi: [10.1086/523645](https://doi.org/10.1086/523645)
- Drozdovskaya, M. N., Walsh, C., Visser, R., Harsono, D., & van Dishoeck, E. F. 2015, *MNRAS*, 451, 3836, doi: [10.1093/mnras/stv1177](https://doi.org/10.1093/mnras/stv1177)
- Dutta, S., Lee, C.-F., Liu, T., et al. 2020, *ApJS*, 251, 20, doi: [10.3847/1538-4365/abba26](https://doi.org/10.3847/1538-4365/abba26)
- Eden, D. J., Liu, T., Kim, K.-T., et al. 2019, *MNRAS*, 485, 2895, doi: [10.1093/mnras/stz574](https://doi.org/10.1093/mnras/stz574)
- Enoch, M. L., Corder, S., Duchêne, G., et al. 2011, *ApJS*, 195, 21, doi: [10.1088/0067-0049/195/2/21](https://doi.org/10.1088/0067-0049/195/2/21)
- Evans, Neal J., I., Yang, Y.-L., Green, J. D., et al. 2022, arXiv e-prints, arXiv:2212.03746, doi: [10.48550/arXiv.2212.03746](https://doi.org/10.48550/arXiv.2212.03746)
- Fazio, G. G., Hora, J. L., Allen, L. E., et al. 2004, *ApJS*, 154, 10, doi: [10.1086/422843](https://doi.org/10.1086/422843)
- Ferreira, J., Dougados, C., & Cabrit, S. 2006, *A&A*, 453, 785, doi: [10.1051/0004-6361:20054231](https://doi.org/10.1051/0004-6361:20054231)
- Fiorellino, E., Tychoniec, L., Cruz-Sáenz de Miera, F., et al. 2023, *ApJ*, 944, 135, doi: [10.3847/1538-4357/aca320](https://doi.org/10.3847/1538-4357/aca320)
- Fiorellino, E., Manara, C. F., Nisini, B., et al. 2021, *A&A*, 650, A43, doi: [10.1051/0004-6361/202039264](https://doi.org/10.1051/0004-6361/202039264)
- Froebrich, D., Schmeja, S., Smith, M. D., & Klessen, R. S. 2006, *MNRAS*, 368, 435, doi: [10.1111/j.1365-2966.2006.10124.x](https://doi.org/10.1111/j.1365-2966.2006.10124.x)
- Furlan, E., Fischer, W. J., Ali, B., et al. 2016, *ApJS*, 224, 5, doi: [10.3847/0067-0049/224/1/5](https://doi.org/10.3847/0067-0049/224/1/5)
- Garrod, R. T., & Herbst, E. 2006, *A&A*, 457, 927, doi: [10.1051/0004-6361:20065560](https://doi.org/10.1051/0004-6361:20065560)
- Garrod, R. T., Widicus Weaver, S. L., & Herbst, E. 2008, *ApJ*, 682, 283, doi: [10.1086/588035](https://doi.org/10.1086/588035)
- Güsten, R., Nyman, L. Å., Schilke, P., et al. 2006, *A&A*, 454, L13, doi: [10.1051/0004-6361:20065420](https://doi.org/10.1051/0004-6361:20065420)
- Herbst, E., & van Dishoeck, E. F. 2009, *ARA&A*, 47, 427, doi: [10.1146/annurev-astro-082708-101654](https://doi.org/10.1146/annurev-astro-082708-101654)
- Hincelin, U., Wakelam, V., Commerçon, B., Hersant, F., & Guilloteau, S. 2013, *ApJ*, 775, 44, doi: [10.1088/0004-637X/775/1/44](https://doi.org/10.1088/0004-637X/775/1/44)
- Hirano, N., Kameya, O., Nakayama, M., & Takakubo, K. 1988, *ApJ*, 327, L69, doi: [10.1086/185142](https://doi.org/10.1086/185142)
- Hsu, S.-Y., Liu, S.-Y., Liu, T., et al. 2020, *ApJ*, 898, 107, doi: [10.3847/1538-4357/ab9f3a](https://doi.org/10.3847/1538-4357/ab9f3a)
- , 2022, *ApJ*, 927, 218, doi: [10.3847/1538-4357/ac49e0](https://doi.org/10.3847/1538-4357/ac49e0)
- Imai, M., et al. 2016, *ApJ*, 830, L37, doi: [10.3847/2041-8205/830/2/L37](https://doi.org/10.3847/2041-8205/830/2/L37)
- Ishihara, D., Onaka, T., Kataza, H., et al. 2010, *A&A*, 514, A1, doi: [10.1051/0004-6361/200913811](https://doi.org/10.1051/0004-6361/200913811)

Table B1. The SPARX simulation results of the nine best-matching YSO models.

Model Name	FWHM _{maj}	FWHM _{min}	PA	$\overline{\text{FWHM}}$	Peak (mJy beam ⁻¹ km s ⁻¹)
G208.68-19.20N1					
3016258_9	0''48	0''46	149°	0''47	583
3014529_9	0''51	0''47	147°	0''49	799
3006540_8	0''52	0''46	160°	0''49	750
3005436_8	0''58	0''48	174°	0''53	474
3005775_8	0''51	0''47	158°	0''49	683
3002402_8	0''54	0''47	178°	0''51	211
3014904_7	0''50	0''45	155°	0''48	351
3010556_9	0''54	0''48	165°	0''51	1057
3008121_8	0''53	0''47	169°	0''50	711
G210.49-19.79W-A					
3001830_7	0''74	0''69	85°	0''71	250
3011394_9	0''74	0''70	90°	0''72	85
3011804_9	0''72	0''69	120°	0''71	270
3018997_7	0''80	0''67	84°	0''73	106
3009709_7	0''82	0''79	90°	0''81	171
3018997_8	0''80	0''79	38°	0''80	95
3017681_9	0''77	0''66	90°	0''71	89
3004153_9	0''67	0''67	32°	0''67	94
3004153_8	0''67	0''65	77°	0''66	108
G211.47-19.27S					
3013227_3	0''72	0''51	72°	0''61	2013
3001398_5	0''73	0''53	74°	0''62	1819
3001398_4	0''77	0''54	72°	0''65	1819
3003853_5	0''68	0''49	77°	0''58	1106
3003853_6	0''66	0''49	78°	0''57	1060
3002254_7	0''78	0''56	74°	0''66	1949
3001398_6	0''71	0''52	75°	0''61	1723
3015663_7	0''83	0''58	76°	0''69	2141
3018117_3	0''73	0''52	71°	0''61	1704

NOTE— The FWHM_{maj}, FWHM_{min}, and PA are the FWHM along the major axis, FWHM along the minor axis, and the position angle exported by the 2D Gaussian fitting. The $\overline{\text{FWHM}}$ is the geometric mean defined as $(\text{FWHM}_{\text{maj}} \times \text{FWHM}_{\text{min}})^{1/2}$. The transition is the CH₃OH-46 transition. The methanol abundance model in SPARX is the “envelope+disk” model.

Jacobsen, S. K., Jørgensen, J. K., Di Francesco, J., et al. 2019, A&A, 629, A29, doi: [10.1051/0004-6361/201833214](https://doi.org/10.1051/0004-6361/201833214)

Jørgensen, J. K., van Dishoeck, E. F., Visser, R., et al. 2009, A&A, 507, 861, doi: [10.1051/0004-6361/200912325](https://doi.org/10.1051/0004-6361/200912325)

Keto, E., & Zhang, Q. 2010, MNRAS, 406, 102, doi: [10.1111/j.1365-2966.2010.16672.x](https://doi.org/10.1111/j.1365-2966.2010.16672.x)

Kim, G., Tatsumatsu, K., Liu, T., et al. 2020, ApJS, 249, 33, doi: [10.3847/1538-4365/aba746](https://doi.org/10.3847/1538-4365/aba746)

Kounkel, M., Covey, K., Suárez, G., et al. 2018, AJ, 156, 84, doi: [10.3847/1538-3881/aad1f1](https://doi.org/10.3847/1538-3881/aad1f1)

Lawrence, A., Warren, S. J., Almaini, O., et al. 2007, MNRAS, 379, 1599, doi: [10.1111/j.1365-2966.2007.12040.x](https://doi.org/10.1111/j.1365-2966.2007.12040.x)

Lee, C.-F., Codella, C., Li, Z.-Y., & Liu, S.-Y. 2019a, ApJ, 876, 63, doi: [10.3847/1538-4357/ab15db](https://doi.org/10.3847/1538-4357/ab15db)

Lee, C.-F., Li, Z.-Y., Ho, P. T. P., et al. 2017, ApJ, 843, 27, doi: [10.3847/1538-4357/aa7757](https://doi.org/10.3847/1538-4357/aa7757)

- Lee, J.-E., Lee, S., Baek, G., et al. 2019b, *NatAs*, 3, 314, doi: [10.1038/s41550-018-0680-0](https://doi.org/10.1038/s41550-018-0680-0)
- Lefèvre, C., Cabrit, S., Maury, A. J., et al. 2017, *A&A*, 604, L1, doi: [10.1051/0004-6361/201730766](https://doi.org/10.1051/0004-6361/201730766)
- Lindberg, J. E., Jørgensen, J. K., Brinch, C., et al. 2014, *A&A*, 566, A74, doi: [10.1051/0004-6361/201322651](https://doi.org/10.1051/0004-6361/201322651)
- Liu, T., Kim, K.-T., Juvela, M., et al. 2018, *ApJS*, 234, 28, doi: [10.3847/1538-4365/aaa3dd](https://doi.org/10.3847/1538-4365/aaa3dd)
- McMullin, J. P., Waters, B., Schiebel, D., Young, W., & Golap, K. 2007, in *Astronomical Data Analysis Software and Systems XVI*, ed. R. A. Shaw, F. Hill, & D. J. Bell, Vol. 376, San Francisco, Astronomical Society of the Pacific (ASP Conference Series)
- Megeath, S. T., Gutermuth, R., Muzerolle, J., et al. 2012, *AJ*, 144, 192, doi: [10.1088/0004-6256/144/6/192](https://doi.org/10.1088/0004-6256/144/6/192)
- Mendoza, S., Cantó, J., & Raga, A. C. 2004, *RMxAA*, 40, 147. <https://ui.adsabs.harvard.edu/abs/2004RMxAA..40..147M>
- Mercimek, S., Codella, C., Podio, L., et al. 2022, *A&A*, 659, A67, doi: [10.1051/0004-6361/202141790](https://doi.org/10.1051/0004-6361/202141790)
- Millar, T. J., & Hatchell, J. 1998, *Faraday Discussions*, 109, 15, doi: [10.1039/a800127h](https://doi.org/10.1039/a800127h)
- Murillo, N. M., Bruderer, S., van Dishoeck, E. F., et al. 2015, *A&A*, 579, A114, doi: [10.1051/0004-6361/201425118](https://doi.org/10.1051/0004-6361/201425118)
- Nazari, P., Tabone, B., Rosotti, G. P., et al. 2022, *A&A*, 663, A58, doi: [10.1051/0004-6361/202142777](https://doi.org/10.1051/0004-6361/202142777)
- Nomura, H., Aikawa, Y., Nakagawa, Y., & Millar, T. J. 2009, *A&A*, 495, 183, doi: [10.1051/0004-6361:200810206](https://doi.org/10.1051/0004-6361:200810206)
- Okoda, Y., Oya, Y., Imai, M., et al. 2022, *ApJ*, 935, 136, doi: [10.3847/1538-4357/ac7ff4](https://doi.org/10.3847/1538-4357/ac7ff4)
- Olguin, F. A., Sanhueza, P., Ginsburg, A., et al. 2022, *ApJ*, 929, 68, doi: [10.3847/1538-4357/ac5bd8](https://doi.org/10.3847/1538-4357/ac5bd8)
- Osorio, M., D'Alessio, P., Muzerolle, J., Calvet, N., & Hartmann, L. 2003, *ApJ*, 586, 1148, doi: [10.1086/367695](https://doi.org/10.1086/367695)
- Oya, Y., Sakai, N., López-Sepulcre, A., et al. 2016, *ApJ*, 824, 88, doi: [10.3847/0004-637X/824/2/88](https://doi.org/10.3847/0004-637X/824/2/88)
- Oya, Y., Sakai, N., Watanabe, Y., et al. 2018, *ApJ*, 863, 72, doi: [10.3847/1538-4357/aac42](https://doi.org/10.3847/1538-4357/aac42)
- Oya, Y., & Yamamoto, S. 2020, *ApJ*, 904, 185, doi: [10.3847/1538-4357/abbe14](https://doi.org/10.3847/1538-4357/abbe14)
- Oya, Y., Sakai, N., Watanabe, Y., et al. 2017, *ApJ*, 837, 174, doi: [ARTN17410.3847/1538-4357/aa6300](https://doi.org/10.3847/1538-4357/aa6300)
- Oya, Y., López-Sepulcre, A., Sakai, N., et al. 2019, *ApJ*, 881, 112, doi: [10.3847/1538-4357/ab2b97](https://doi.org/10.3847/1538-4357/ab2b97)
- Pilbratt, G. L., Riedinger, J. R., Passvogel, T., et al. 2010, *A&A*, 518, L1, doi: [10.1051/0004-6361/201014759](https://doi.org/10.1051/0004-6361/201014759)
- Planck, C., Ade, P. A. R., Aghanim, N., et al. 2016, *A&A*, 594, A28, doi: [10.1051/0004-6361/201525819](https://doi.org/10.1051/0004-6361/201525819)
- Poglitsch, A., Waelkens, C., Geis, N., et al. 2010, *A&A*, 518, L2, doi: [10.1051/0004-6361/201014535](https://doi.org/10.1051/0004-6361/201014535)
- Price-Whelan, A. M., Sipőcz, B. M., Günther, H. M., et al. 2018, *AJ*, 156, 123, doi: [10.3847/1538-3881/aabc4f](https://doi.org/10.3847/1538-3881/aabc4f)
- Pringle, J. E. 1981, *ARA&A*, 19, 137, doi: [10.1146/annurev.aa.19.090181.001033](https://doi.org/10.1146/annurev.aa.19.090181.001033)
- Rieke, G. H., Young, E. T., Engelbracht, C. W., et al. 2004, *ApJS*, 154, 25, doi: [10.1086/422717](https://doi.org/10.1086/422717)
- Robitaille, T. P., Whitney, B. A., Indebetouw, R., & Wood, K. 2007, *ApJS*, 169, 328, doi: [10.1086/512039](https://doi.org/10.1086/512039)
- Robitaille, T. P., Whitney, B. A., Indebetouw, R., Wood, K., & Denzmore, P. 2006, *ApJS*, 167, 256, doi: [10.1086/508424](https://doi.org/10.1086/508424)
- Sahu, D., Liu, S. Y., Su, Y. N., et al. 2019, *ApJ*, 872, 196, doi: [ARTN19610.3847/1538-4357/aaffda](https://doi.org/10.3847/1538-4357/aaffda)
- Sakai, N., Sakai, T., Hirota, T., & Yamamoto, S. 2008, *ApJ*, 672, 371, doi: [Doi10.1086/523635](https://doi.org/10.1086/523635)
- Seale, J. P., & Looney, L. W. 2008, *ApJ*, 675, 427, doi: [10.1086/526766](https://doi.org/10.1086/526766)
- Shirley, Y. L., Evans, Neal J., I., Rawlings, J. M. C., & Gregersen, E. M. 2000, *ApJS*, 131, 249, doi: [10.1086/317358](https://doi.org/10.1086/317358)
- Siringo, G., Kreysa, E., Kovács, A., et al. 2009, *A&A*, 497, 945, doi: [10.1051/0004-6361/200811454](https://doi.org/10.1051/0004-6361/200811454)
- Siringo, G., Kreysa, E., De Breuck, C., et al. 2010, *The Messenger*, 139, 20. <https://ui.adsabs.harvard.edu/abs/2010Msngr.139...20S>
- Stutz, A. M., Tobin, J. J., Stanke, T., et al. 2013, *ApJ*, 767, 36, doi: [10.1088/0004-637X/767/1/36](https://doi.org/10.1088/0004-637X/767/1/36)
- Tabone, B., Cabrit, S., Bianchi, E., et al. 2017, *A&A*, 607, L6, doi: [10.1051/0004-6361/201731691](https://doi.org/10.1051/0004-6361/201731691)
- Tatematsu, K., Liu, T., Ohashi, S., et al. 2017, *ApJS*, 228, 12, doi: [10.3847/1538-4365/228/2/12](https://doi.org/10.3847/1538-4365/228/2/12)
- Tatematsu, K., Liu, T., Kim, G., et al. 2020, *ApJ*, 895, 119, doi: [10.3847/1538-4357/ab8d3e](https://doi.org/10.3847/1538-4357/ab8d3e)
- Tobin, J. J., Stutz, A. M., Megeath, S. T., et al. 2015, *ApJ*, 798, 128, doi: [10.1088/0004-637X/798/2/128](https://doi.org/10.1088/0004-637X/798/2/128)
- Tobin, J. J., Sheehan, P. D., Megeath, S. T., et al. 2020, *ApJ*, 890, 130, doi: [10.3847/1538-4357/ab6f64](https://doi.org/10.3847/1538-4357/ab6f64)
- Ulrich, R. K. 1976, *ApJ*, 210, 377, doi: [10.1086/154840](https://doi.org/10.1086/154840)
- van der Marel, N., Booth, A. S., Leemker, M., van Dishoeck, E. F., & Ohashi, S. 2021, *A&A*, 651, L5, doi: [10.1051/0004-6361/202141051](https://doi.org/10.1051/0004-6361/202141051)
- van Gelder, M. L., Tabone, B., Tychoniec, Ł., et al. 2020, *A&A*, 639, A87, doi: [10.1051/0004-6361/202037758](https://doi.org/10.1051/0004-6361/202037758)
- van Gelder, M. L., Nazari, P., Tabone, B., et al. 2022, *A&A*, 662, A67, doi: [10.1051/0004-6361/202142769](https://doi.org/10.1051/0004-6361/202142769)
- van 't Hoff, M. L. R., Persson, M. V., Harsono, D., et al. 2018, *A&A*, 613, A29, doi: [10.1051/0004-6361/201731656](https://doi.org/10.1051/0004-6361/201731656)
- van 't Hoff, M. L. R., Harsono, D., Tobin, J. J., et al. 2020, *ApJ*, 901, 166, doi: [10.3847/1538-4357/abb1a2](https://doi.org/10.3847/1538-4357/abb1a2)
- Vastel, C., Alves, F., Ceccarelli, C., et al. 2022, *A&A*, 664, A171, doi: [10.1051/0004-6361/202243414](https://doi.org/10.1051/0004-6361/202243414)
- Watson, D. M. 2020, *RNAAS*, 4, 88, doi: [10.3847/2515-5172/ab9df4](https://doi.org/10.3847/2515-5172/ab9df4)

- Werner, M. W., Roellig, T. L., Low, F. J., et al. 2004, *ApJS*, 154, 1, doi: [10.1086/422992](https://doi.org/10.1086/422992)
- Whitney, B. A., Wood, K., Bjorkman, J. E., & Cohen, M. 2003a, *ApJ*, 598, 1079, doi: [10.1086/379068](https://doi.org/10.1086/379068)
- Whitney, B. A., Wood, K., Bjorkman, J. E., & Wolff, M. J. 2003b, *ApJ*, 591, 1049, doi: [10.1086/375415](https://doi.org/10.1086/375415)
- Wright, E. L., Eisenhardt, P. R. M., Mainzer, A. K., et al. 2010, *AJ*, 140, 1868, doi: [10.1088/0004-6256/140/6/1868](https://doi.org/10.1088/0004-6256/140/6/1868)
- Wu, P.-F., Takakuwa, S., & Lim, J. 2009, *ApJ*, 698, 184, doi: [10.1088/0004-637X/698/1/184](https://doi.org/10.1088/0004-637X/698/1/184)
- Yamamura, I. 2010, in 38th COSPAR Scientific Assembly, Vol. 38, 2. <https://ui.adsabs.harvard.edu/abs/2010cosp...38.2496Y>
- Yang, Y.-L., Sakai, N., Zhang, Y., et al. 2021, *ApJ*, 910, 20, doi: [10.3847/1538-4357/abdfd6](https://doi.org/10.3847/1538-4357/abdfd6)
- Yen, H.-W., Koch, P. M., Takakuwa, S., et al. 2017, *ApJ*, 834, 178, doi: [10.3847/1538-4357/834/2/178](https://doi.org/10.3847/1538-4357/834/2/178)
- Yen, H.-W., Takakuwa, S., Koch, P. M., et al. 2015, *ApJ*, 812, 129, doi: [10.1088/0004-637X/812/2/129](https://doi.org/10.1088/0004-637X/812/2/129)
- Yen, H.-W., Takakuwa, S., & Ohashi, N. 2010, *ApJ*, 710, 1786, doi: [10.1088/0004-637X/710/2/1786](https://doi.org/10.1088/0004-637X/710/2/1786)
- Yi, H.-W., Lee, J.-E., Liu, T., et al. 2018, *ApJS*, 236, 51, doi: [10.3847/1538-4365/aac2e0](https://doi.org/10.3847/1538-4365/aac2e0)
- Yoneda, H., Tsukamoto, Y., Furuya, K., & Aikawa, Y. 2016, *ApJ*, 833, 105, doi: [10.3847/1538-4357/833/1/105](https://doi.org/10.3847/1538-4357/833/1/105)